AIAA SciTech Forum
January 3-7, 2022, San Diego, CA & Virtual
AIAA SCITECH 2022 Forum

10.2514/6.2022-1212

Effect of Distributed Surface Roughness on the Stability of High-Speed Flows

Bijaylakshmi Saikia *[1,2] and Christoph Brehm †[1,2]
[1]*Department of Mechanical Engineering, University of Kentucky, Lexington, KY 40506, USA*
[2]*Department of Aerospace Engineering, University of Maryland, College Park, MD 20742, USA*

A parametric variation of height and wavelength of distributed sinusoidal roughness is carried out to study their individual effect on the stability of a Mach 5.35 flat plate flow. Four different cases are considered with a relative roughness amplitude between 10 and 44 percent of the boundary layer height to examine the effect of varying roughness height. Another four cases are chosen to investigate the effects of the roughness wavelength which varies between roughly 0.44 to 3.55 times the second mode wavelength. The presence of the surface roughness led to strong variations in the mean flow quantities compared to the smooth wall case causing local acceleration and deceleration of the flow. The steady mean flow field showed supersonic wave patterns generated by the roughness elements emanating into the freestream. The disturbance flow analysis in the frequency domain based on wall pressure data showed that the flow was destabilized for the fixed wavelength cases with variable roughness heights. The shortest wavelength case from the fixed roughness height cases was the only one that showed a stabilization of the flow. For the range of wavelengths considered, the level of destabilization was found to be a strong function of the roughness wavelength. For all roughness cases, a shift towards lower frequencies was observed in the pressure amplitude plots. For the higher roughness height and larger wavelength cases, a second region of amplified modes at higher frequencies was noted which may suggest destabilization of a higher Mach mode or the occurrence of a different instability mechanism. To gain insight into the energy transfer mechanisms from the mean flow to the disturbance flow, an energy budget analysis is also performed.

I. Introduction

The thermal protection system (TPS) in hypersonic-cruise and atmospheric-entry vehicles can be designed to pyrolyze and ablate when subjected to an intense aerothermal heating environment during their operation to protect the underlying structure and the payload. Gaseous species are released due to the internal decomposition of the solid during pyrolysis and recession generates surface roughness at the heat-shield surface. Both of these processes can have a dramatic impact on the laminar to the turbulent transition process [1, 2].

The effect of surface roughness and ablation are often coupled and to develop nose-tips for slender military reentry vehicles, this complex problem was extensively researched in the 1960s and 1970s. Schneider presented an extensive review of experimental results summarizing the effects of of isolated and distributed surface roughness on hypersonic blunt-body transition in Ref. [2]. A significant amount of work has been carried out to analyze how surface roughness affects the boundary layer transition both for isolated roughness elements [3, 4] as well as for distributed roughness [5–7]. Marxen et al. [8] reported that for a Mach 4.8 flat plate boundary layer flow, the stability characteristics are significantly altered by the presence of roughness with increased amplification and damping depending on the disturbance frequency. Egorov et al. [9] numerically studied the stabilization of supersonic boundary layer flows over a shallow grooved wavy plate at Mach 5.9. It was found that the wavy wall can damp the perturbation in a wide frequency range. In another study, Duan et al. [10] applied a third-order cut-cell method to simulate roughness-induced receptivity for a hypersonic flow over a flat plate with a blowing and suction slot placed near the leading edge. They inferred that by placing the 2-D roughness element downstream of the synchronization location of the slow and the fast mode, the disturbances can be damped considerably. In a similar work, Duan et al. [11] noted that a roughness element with a height equal to half of the boundary layer thickness placed at the right location can delay the transition process. Fong et al. [12] investigated the effect of two-dimensional roughness on perturbation growth over a Mach 5.92 flat plate boundary

*Postdoctoral Researcher and AIAA Member.
†Assistant Professor and AIAA Member.

layer. They mentioned that if a roughness element is placed downstream of the synchronization point, perturbations at frequencies higher than the synchronization frequency are damped and perturbations at lower frequencies are amplified. They also revealed that if the roughness height is smaller than the local boundary layer thickness, the placement of the roughness element determines if amplification or damping will occur. In a recent work carried out using direct numerical simulation (DNS) and parabolized stability equations (PSE), Fong and Zhong [13] commented that the effect of roughness on Mack's second mode is a result of the alteration of the mean flow and, the synchronization location is an important parameter which determines the effect of the roughness. Fong et al. [14] also performed a parametric variation of roughness parameters including roughness height, width, and spacing between roughness elements. They showed that when the spacing between the roughness elements is ten times the roughness width, the amplification rate of the second mode reduces for a large range of disturbance frequencies. Zhou et al. [15] examined the effects of wavy-wall wave number, depth, and streamwise location on the Mach 6 hypersonic boundary-layer stability. They reported that the wavy wall with multiple wavenumbers can suppress the second-mode growth significantly through the presence of multiple separation regions as opposed to the case of a wavy wall with a single wave number which amplifies the second mode which they attributed to a shorter recirculation region. The influence of different wavy surface shapes such as arc, saw-tooth, and triangular elements was studied for a Mach 5.95 flow by Poplavskaya and Kirilovskiy [16].

Recently, Giovanni & Stemmer [17, 18] investigated the development of unsteady disturbance in a Mach 20 flow over a capsule-like hemispherical geometry with pseudo-random distributed roughness. The largest amplification of the disturbance was observed for a crossflow-type vortex developing in the wake of the highest skewed protuberance of the roughness patch. They also studied the influence of high-temperature gas effects on the laminar-turbulent transition induced by a patch of distributed roughness. Iyer et al. [6] conducted direct numerical simulations for a Mach 2.9 flow past a flat plate with distributed roughness. They noted that the cumulative effect of multiple roughness elements is to decelerate the near-wall fluid, and set up inflectional velocity profiles. Recently, Shrestha & Candler [7] compared the instability mechanisms of a Mach 5.65 laminar boundary layer tripped by an isolated and span-wise array of diamond-shaped trips using direct numerical simulations. The source of instability was attributed to the interaction between the shear layers and the counter-rotating stream wise vortices downstream of both trip configurations.

In addition to the numerical studies, various experiments were conducted to understand the effects of roughness on flow transition. Holloway and Sterrett [19] studied the effects of controlled three-dimensional surface roughness (spheres) on the boundary-layer transition at Mach 6. It was reported that surface roughness of height less than the boundary-layer thickness can delay the transition process. The experimental data also predicted that to trip the boundary layer flow fully, roughness heights of approximately twice the boundary-layer thickness at the roughness location are required. Recently, Fujii [20] carried out an experimental investigation at the JAXA 0.5 m hypersonic wind tunnel using a 5 degree half-angle sharp cone at a freestream Mach number of 7.1 and a wide range of stagnation conditions. He mentioned that a wavy wall with a wavelength of twice the boundary layer thickness located well upstream of the breakdown region can delay transition.

The aforementioned studies were mostly focused on the regular roughness shapes, whereas ablation can create random irregular surface patterns. The effect of irregular roughness shapes on the transition process is largely unknown. The flight tests and the experiments can rarely provide a thorough understanding of physical mechanisms by decoupling the coexisting physical phenomena. Therefore to understand the role of distributed roughness on flow stability, we will conduct a numerical investigation by varying the roughness height and the wavelength. Isolating one roughness parameter from another will provide a thorough understanding of how different lengths and heights of the roughness elements can affect the transition process at high-Mach number conditions. For this, a Mach 5.35 flow over a wavy flat plate will be simulated and by comparing with a smooth flat plate at the same conditions, we will study the effect of varying roughness height and the wavelength.

The organization of the paper is as follows. The governing equations for the mean flow and for the small-amplitude disturbances are introduced in section II. The test cases constructed to study the effects of roughness parameters are discussed in section III. The effects of varying the roughness amplitude on the mean flow and the disturbance flow field is analyzed in section IV. The next section V addresses the effects of a variation in the roughness wavelength. A summary of this work is provided in section VI.

II. Governing Equations

The mean flow field is computed by solving the compressible Navier-Stokes equations, which can be written as,

$$\frac{\partial \mathbf{U}}{\partial t} + \frac{\partial \mathbf{F_i}}{\partial x_i} + \frac{\partial \mathbf{F_{v_i}}}{\partial x_i} = \mathbf{0}; \tag{1}$$

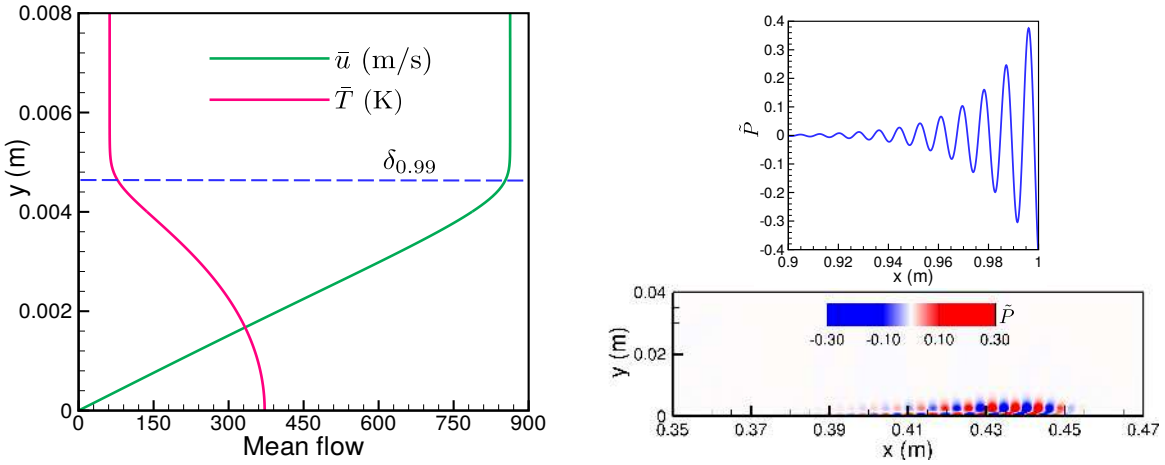

(a) Mean flow velocity and temperature

(b) Disturbance pressure

Fig. 1 (a) Variation of the stream wise velocity and mean flow temperature along the wall-normal direction extracted at x=1 m of the smooth flat plate, with the blue dashed line indicating the boundary layer thickness. (b) Line plot of surface pressure along the wall and contours of disturbance pressure visualizing the second mode dominated wave-packet above the flat plate at Mach 5.35.

where,

$$\mathbf{U} = \begin{bmatrix} \rho \\ \rho u \\ \rho v \\ E \end{bmatrix}; \quad \mathbf{F} = \begin{bmatrix} \rho u_i \\ \rho u u_i + P\delta_{1i} \\ \rho v u_i + P\delta_{2i} \\ (E+P)u_i \end{bmatrix}; \quad \mathbf{F_v} = \begin{bmatrix} 0 \\ -\tau_{1i} \\ -\tau_{2i} \\ -\kappa \frac{\partial T}{\partial x_i} - \tau_{ij} u_j \end{bmatrix}.$$

Here, $\mathbf{U}$ is the solution vector of the conservative variables, $\mathbf{F}$ and $\mathbf{F_v}$ are the inviscid and viscous fluxes, respectively. The first row in (1) corresponds to the continuity equation. The next two rows of (1) correspond to the momentum equations in the x- and y-directions. u, v, P, and τ_{ij} are the x- and y-velocity, thermodynamic pressure, and components of stress tensor, respectively. The total energy equation is listed in the last row of (1) where E consists of internal energy and the kinetic energy of the gas. The heat conduction is evaluated by using Fourier's law of heat conduction, where κ represents the thermal conductivity.

In this work, only small disturbances introduced into a perfect gas flow are considered. The equations to be solved are the linear disturbance equations (LDE), and to derive them we first recast the conservative form of the Navier-Stokes equations (1) into a primitive variable form by using a conservative to a primitive transformation matrix ($\partial\tilde{\mathbf{U}}/\partial\tilde{\mathbf{Q}}$). The instantaneous state vector of the primitive variables $\mathbf{Q} = [P, u, v, T]^T$ is decomposed into a steady mean flow $\bar{\mathbf{Q}}$ and an unsteady disturbance quantity $\tilde{\mathbf{Q}}$. Since the mean flow satisfies the Navier-Stokes equations, it can be subtracted from the instantaneous state vector $\mathbf{Q}$ to obtain the governing equations for the disturbances. After neglecting the higher order terms in the disturbances, the governing equation for the linear disturbances can be written as,

$$\frac{\partial \tilde{\mathbf{U}}}{\partial \tilde{\mathbf{Q}}} \frac{\partial \tilde{\mathbf{Q}}}{\partial t} + \frac{\partial \tilde{\mathbf{F}}_\mathbf{i}}{\partial x_i} + \frac{\partial \tilde{\mathbf{F}}_{\mathbf{v_i}}}{\partial x_i} = \mathbf{0}; \tag{2}$$

$$\tilde{\mathbf{U}} = \begin{bmatrix} \tilde{\rho} \\ \tilde{\rho}\bar{u} + \bar{\rho}\tilde{u} \\ \tilde{\rho}\bar{v} + \bar{\rho}\tilde{v} \\ \tilde{E} \end{bmatrix}; \quad \tilde{\mathbf{F}} = \begin{bmatrix} \tilde{\rho}\bar{u} + \bar{\rho}\tilde{u} \\ \bar{\rho}\bar{u}\tilde{u}_i + \bar{\rho}\bar{u}_i\tilde{u} + \tilde{\rho}\bar{u}\bar{u}_i + \tilde{P}\delta_{1i} \\ \bar{\rho}\bar{v}\tilde{u}_i + \bar{\rho}\bar{u}_i\tilde{v} + \tilde{\rho}\bar{v}\bar{u}_i + \tilde{P}\delta_{2i} \\ (\bar{E}+\tilde{P})\,\tilde{u}_i + (\tilde{E}+\tilde{P})\,\bar{u}_i \end{bmatrix}; \quad \tilde{\mathbf{F}}_\mathbf{v} = \begin{bmatrix} 0 \\ -\tilde{\tau}_{1i} \\ -\tilde{\tau}_{2i} \\ -\tilde{\kappa}\frac{\partial \bar{T}}{\partial x_i} - \bar{\kappa}\frac{\partial \tilde{T}}{\partial x_i} - \tilde{\tau}_{ij}\bar{u}_j - \bar{\tau}_{ij}\tilde{u}_j \end{bmatrix}.$$

The primitive state vector used here to represent the disturbance flow is $\mathbf{Q}' = [p', u', v', T']^T$ with tilde denotes the disturbance quantities and the overbar is used for the mean flow. The total energy of the disturbance can be written as

Cases	Wavelength (m)	Percent of 2^{nd} mode wavelength	Amplitude (m)	Percent of boundary layer height
W2A1	8×10^{-3}	88.9	4.8×10^{-4}	10.4
W2A2	8×10^{-3}	88.9	9.6×10^{-4}	20.9
W2A3	8×10^{-3}	88.9	1.5×10^{-3}	32.6
W2A4	8×10^{-3}	88.9	2×10^{-3}	43.5

Table 1 Cases constructed to study the effects of varying roughness amplitude with fixed wavelength.

$\tilde{E} = \bar{\rho}C_v\tilde{T} + \tilde{\rho}C_v\bar{T} + \bar{\rho}\bar{u}\tilde{u} + \bar{\rho}\bar{v}\tilde{v} + 0.5\tilde{\rho}(\bar{u}^2 + \bar{v}^2)$. The specific heat and the specific gas constant are represented by C_v and R, respectively. For a more detailed description of the linear disturbance equations refer to Brown et. al. [21, 22].

III. Test cases

The test cases considered in this work to study the effect of a parametric variation of distributed roughness are designed based on the boundary layer thickness and the second mode wavelength at the end of the computational domain of a 1 m smooth flat plate. For this, we first computed a Mach 5.35 flow over a smooth flat plate with a free-stream temperature of 64.316 K and a unit Reynolds number of 14.356×10^6 m^{-1}. The steady mean flow field is computed by solving the compressible Navier-Stokes equations presented in Eq. 1. The convective fluxes are calculated using a 5^{th} order weighted essentially non-oscillatory (WENO) scheme [23], with Rusanov flux splitting and the viscous fluxes are computed by a second-order central difference method. A first-order backward-difference scheme is used to advance the governing equations in pseudo-time until the steady-state is reached. At the inflow boundary, a self-similarity boundary layer profile is imposed, and no-slip and adiabatic boundary conditions are applied at the surface of the flat plate. An extrapolation boundary condition is applied at the outflow as well as on the top boundary of the domain.

The mean flow velocity and temperature profiles extracted at $x = 0.4$ m corresponding to the smooth flat plate are plotted along the boundary layer in Fig. 1(a). The dashed blue line in the figure marks the boundary layer thickness which is around $\delta_{0.99} = 0.0046$ m. The amplitude of the roughness elements is chosen based on this value, and four different test cases are designed by varying the roughness height but with a fixed wavelength to investigate the effect of variation of the roughness amplitude, which are mentioned in Table 1.

Next, to obtain the wavelength of the second mode corresponding to a smooth flat plate, we computed the disturbance flow field by solving the linear disturbance equations (2). The time-integration has been carried out using a 2^{nd} order Runge-Kutta scheme. Similar to the mean flow field, an extrapolation boundary condition is applied at the outflow and on the top boundary. At the inlet, Dirichlet boundary conditions are imposed on the primitive variables. At the wall, no-slip, isothermal, and no penetration conditions are applied, except at the forcing location. The forcing location spans between $x = [0.02 - 0.026]$ m in the steam-wise direction, where a broadband pulse is introduced into the flow field via wall-forcing through the wall-normal velocity component in terms of a boundary condition. The pulse is centered at 100 kHz to ensure that a second-mode dominated wave packet can be generated with pulse forcing. The wall-forcing term is composed of a spatial and a temporal component which can be written as,

$$G(x,t) = \begin{cases} A\cos(\pi \mathrm{x_h})^3 \sin(-\frac{2\pi \mathrm{t}}{\mathrm{T_f}}); & t \le T_f, \\ 0; & t > T_f. \end{cases} \tag{3}$$

$$x_h = \frac{x - 0.5(x_s + x_e)}{x_e - x_s}.$$

Here, x_s and x_e represent the start and end location of the pulse in the stream wise direction. The amplitude of the pulse is denoted by A, T_f is the disturbance period and t is the time.

A snapshot of the instantaneous disturbance flow field over the smooth flat plate is presented in Fig. 1(b) showing pressure contours, with the red and blue contours denoting the positive and negative values of $\tilde{P}$, respectively. The pulse with a forcing frequency centered around 100 kHz excites the second mode instability in the flow which is identified from the two-cell structures near the wall. The variation of the disturbance pressure is plotted at the end of the

Cases	Wavelength (m)	Percent of 2^{nd} mode wavelength	Amplitude (m)	Percent of boundary layer height
W1A2	4×10^{-3}	44.4	9.6×10^{-4}	20.9
W2A2	8×10^{-3}	88.9	9.6×10^{-4}	20.9
W3A2	16×10^{-3}	177.8	9.6×10^{-4}	20.9
W4A2	32×10^{-3}	355.6	9.6×10^{-4}	20.9

Table 2 Cases constructed to study the effects of varying roughness wavelength with fixed amplitude.

computational domain in the top panel of Fig. 1(b). From the figure, it can be inferred that the dominant second mode attains a wavelength of around $\lambda = 0.009$ m at the end of the flat plate. The test cases presented in Table 1 are designed to have a fixed wavelength of around 89% of the second mode wavelength. Next, to study the effect of a change in the roughness wavelength, we have considered four test cases in Table 2, where the wavelength of the distributed roughness is varied as a function of the second mode wavelength (= 0.009 m), keeping the roughness height fixed at $A = 0.00096$ m.

To introduce the roughness at the surface of the smooth flat plate, we have used the following analytical expression,

$$y_{\text{wavy}} = y_{\text{smooth}} + 0.25 \max(A - y_{\text{smooth}}, 0) \cos\left(\frac{2\pi(x - x_s)}{\lambda}\right) - 0.25A,$$

where y_{wavy} and y_{smooth} denote the wall-normal distance for the flat plate with and without roughness respectively. The roughness elements begin at $x_s = 0.026$ m and end at 0.978 m, whereas the computational domain spans between $x = [0.01, 1]$ m. The top boundary is located at $y = 0.26$ m and the lower boundary is a function of the roughness height. After a thorough grid convergence study, the stream wise and the wall-normal directions are discretized with 8000 and 500 grid points, respectively. Grid points are uniform in the stream wise direction, whereas in the wall-normal direction, points are clustered near the wall, with a minimum wall-normal spacing of $\Delta y_w = 5 \times 10^{-6}$ m. A schematic of the wavy wall grid **W2A2** is displayed in Fig. 2, after skipping five grid points in both the directions. In the next section, we will discuss the effects of varying the roughness amplitude on the mean flow field.

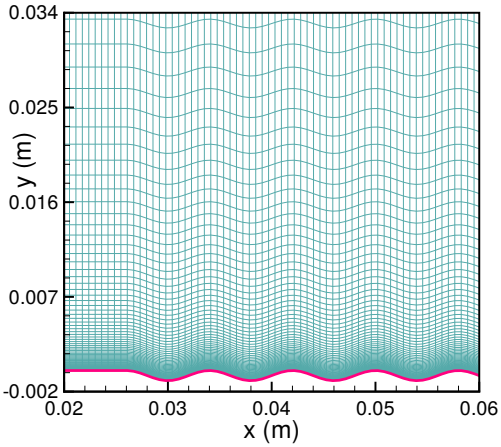

Fig. 2 Computational grid for the wavy wall case W2A2.

IV. Effects of variation of roughness height

In the case of hypersonic flows, it was reported that very large roughness heights are required to affect the transition process [24]. Duan et al. [11] found that a roughness element with a height equal to half of the boundary layer thickness might delay the transition process. However, if the roughness height is much less than the local boundary layer thickness, the placement of the roughness element, whether it is upstream or downstream of the synchronization point will determine if amplification or damping will occur [12]. The experiments conducted by Holloway and Sterrett [19] at Mach 6 also confirmed that to trip the boundary layer flow fully, roughness heights of approximately twice the boundary-layer thickness at the roughness location are required. Although the effect of a single roughness is easily perceived, more physical insight is still required to understand the effects of distributed roughness. Therefore, in this section we will vary the amplitude of the distributed roughness elements from 10.4% to 43.5% of the boundary layer thickness and study its affect on the mean and the disturbance flow field.

A. Simulation of the mean flow field

The steady mean flow field corresponding to the four test cases presented in Table 1 is obtained by solving the compressible Navier-Stokes equations. A sub domain of the simulated pressure flow field is shown in Fig. 3. When the supersonic flow reaches the first roughness element at $x = 0.026$ m, due to a smooth increase in the flow area, expansion

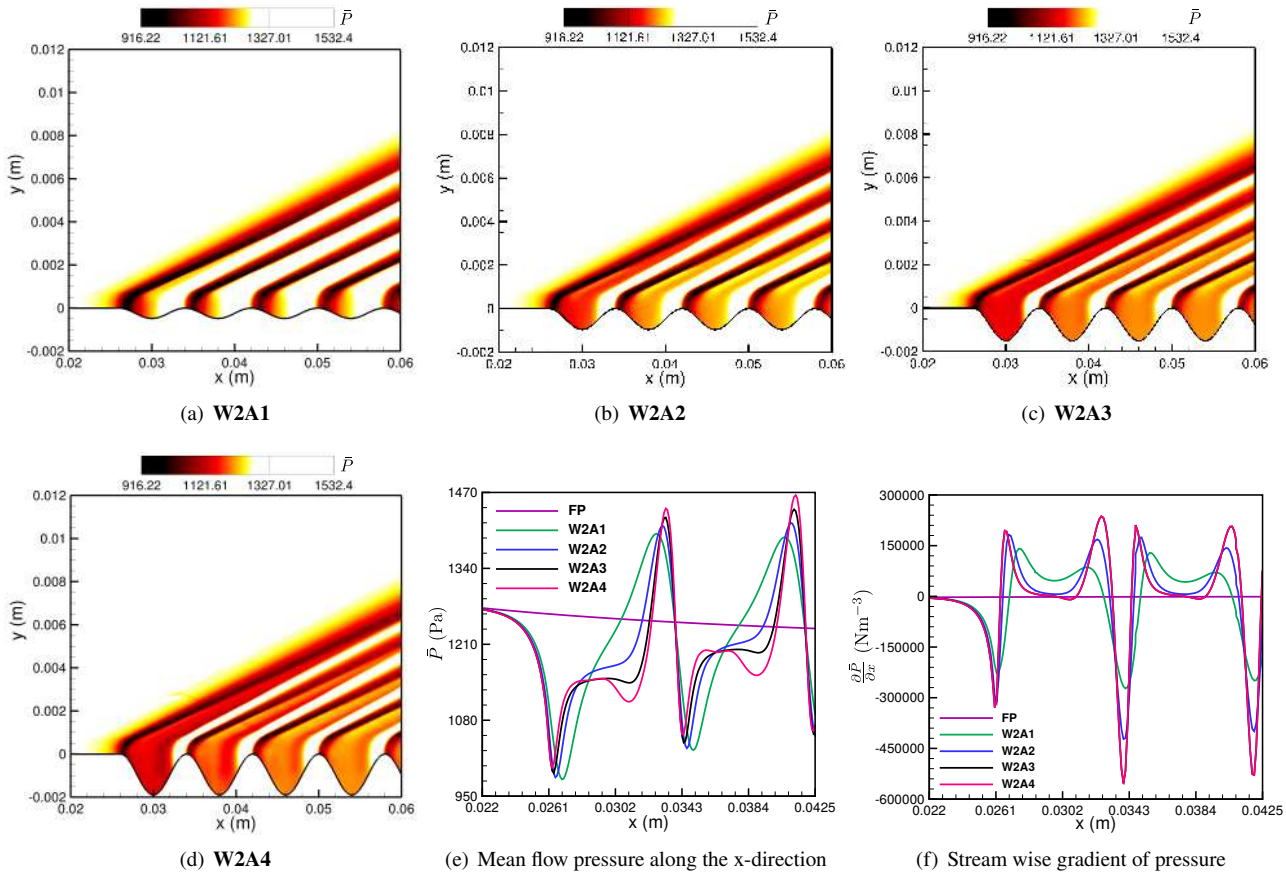

(a) **W2A1** (b) **W2A2** (c) **W2A3**

(d) **W2A4** (e) Mean flow pressure along the x-direction (f) Stream wise gradient of pressure

Fig. 3 (a)-(d) Contours of pressure showing the effects of varying the roughness amplitude on the mean flow field. Variation of (e) mean flow pressure and (f) its stream wise gradient above the first two roughness elements extracted at y=0 m.

fans are created. Across the expansion fan, flow accelerates, while reducing the temperature and the static pressure of the flow and the lowest values of these two quantities are observed in the dark black region. As the amplitude of the roughness elements is increased, the strength of the expansion fan becomes mildly stronger, which can be seen from a small reduction in the peak value of $\bar{P}$ at around $x = 0.0261$ m in Fig. 3(e). The variation of mean flow pressure along the stream wise direction is shown in Fig. 3(e) for the first two roughness elements at $y = 0$ m. Moving across a single roughness element, pressure and the temperature slowly increase over the constricted area which can be identified from the change of contour colors from red to white. The highest values of these two quantities are observed slightly downstream of the crest of the roughness elements, where flow compression creates compression waves. The largest roughness height leads to the highest pressure recovery which can be seen around $x = 0.033$ m for the first roughness element (see Fig. 3(e)). Compared to the smooth wall case, the presence of expansion and compression waves leads to a strong variation of pressure in the wavy wall cases. The variation of the stream wise gradient of mean flow pressure in Fig. 3(f) shows the presence of adverse pressure gradient inside the roughness elements for the amplitude varying cases. This leads to separated flow inside the cavities, which is shown by the blue streamlines in Fig. 4. For all the amplitude varying cases considered here, the separation region extends throughout the entire length of the roughness elements similar to what is typically classified as d-type roughness. The red contours in Fig. 4 represent the zero contours of the inflectional profile ($\frac{\partial}{\partial y}(\rho \frac{\partial U}{\partial y}) = 0$), which is an indication of the presence of inviscid instability in the flow field for all the amplitude varying cases.

A comparison of the boundary layer profiles between the smooth wall case and the amplitude varying wavy wall cases is presented in Fig. 5. For the smooth flat plate (FP), the data is extracted at $x = 0.4$ m, whereas, the profiles for the rough wall cases are shown after averaging over a roughness wavelength between $x = 0.396$ m and 0.404 m. Since

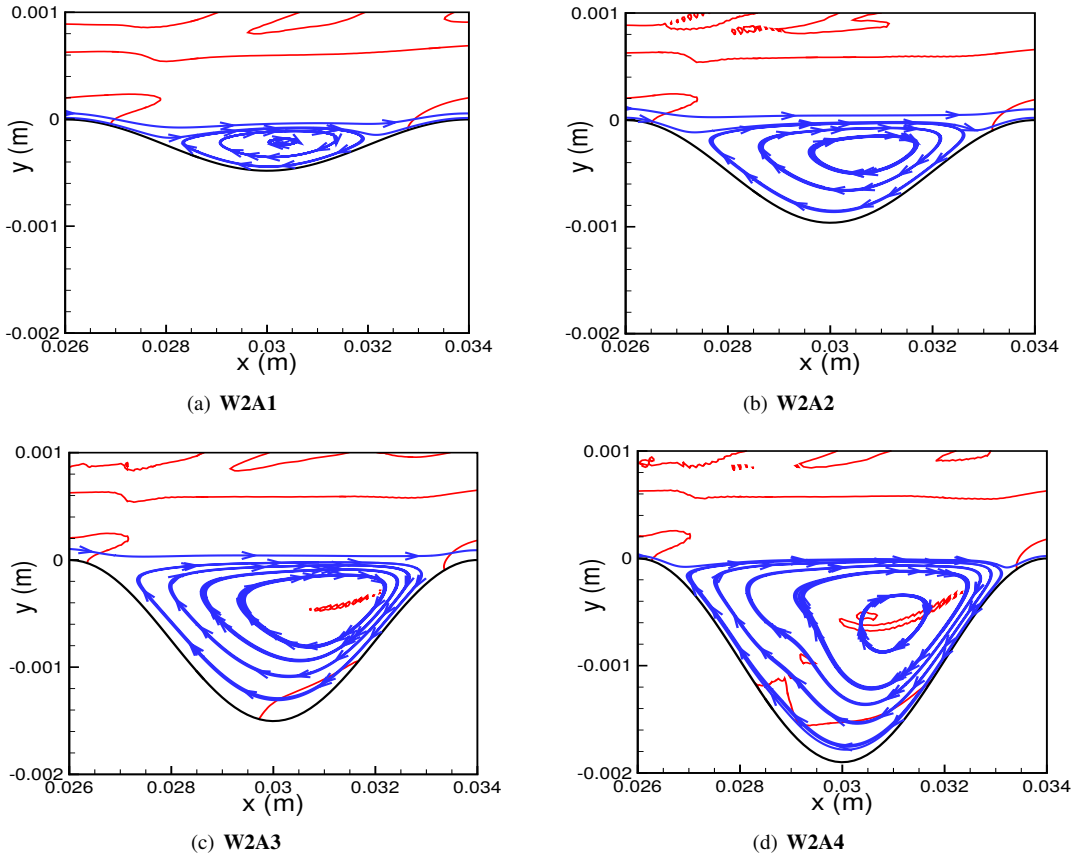

(a) **W2A1** (b) **W2A2**

(c) **W2A3** (d) **W2A4**

Fig. 4 Streamlines visualizing regions of flow separation and zero contours of inflectional profile $\frac{\partial}{\partial y}(\bar{\rho}\frac{\partial \bar{u}}{\partial y})$ for the four amplitude varying cases from Table 1.

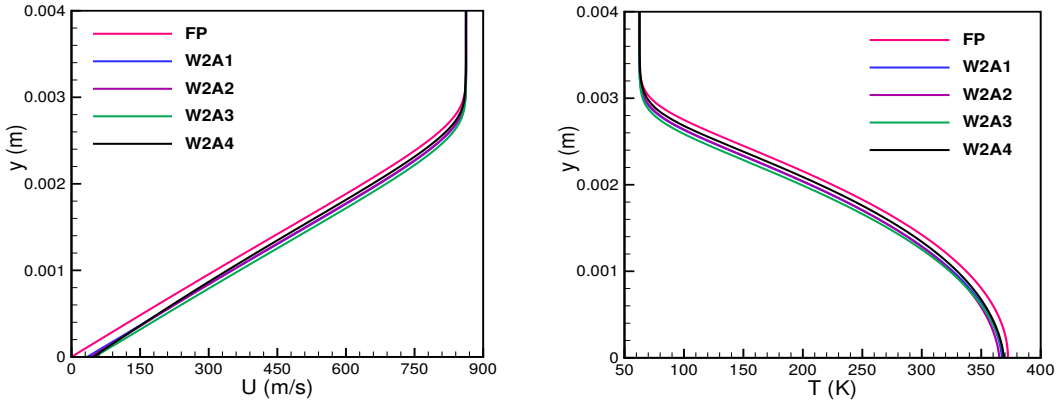

(a) stream wise velocity (b) Temperature

Fig. 5 Comparison of (a) velocity and (b) temperature profiles averaged over a roughness wavelength for the four amplitude varying cases compared with the smooth wall data extracted at x=0.4 m.

the boundary layer profiles corresponding to the wavy wall cases are extracted above the separation bubble starting at $y = 0$ m, none of the mean flow velocity profiles in Fig. 5(a) shows negative values. Compared to the smooth wall case, all the wavy wall cases display a slightly higher velocity throughout the boundary layer, however, there is no noticeable difference in the boundary layer thickness. A comparison of mean flow temperature profiles in Fig. 5(b) shows that the

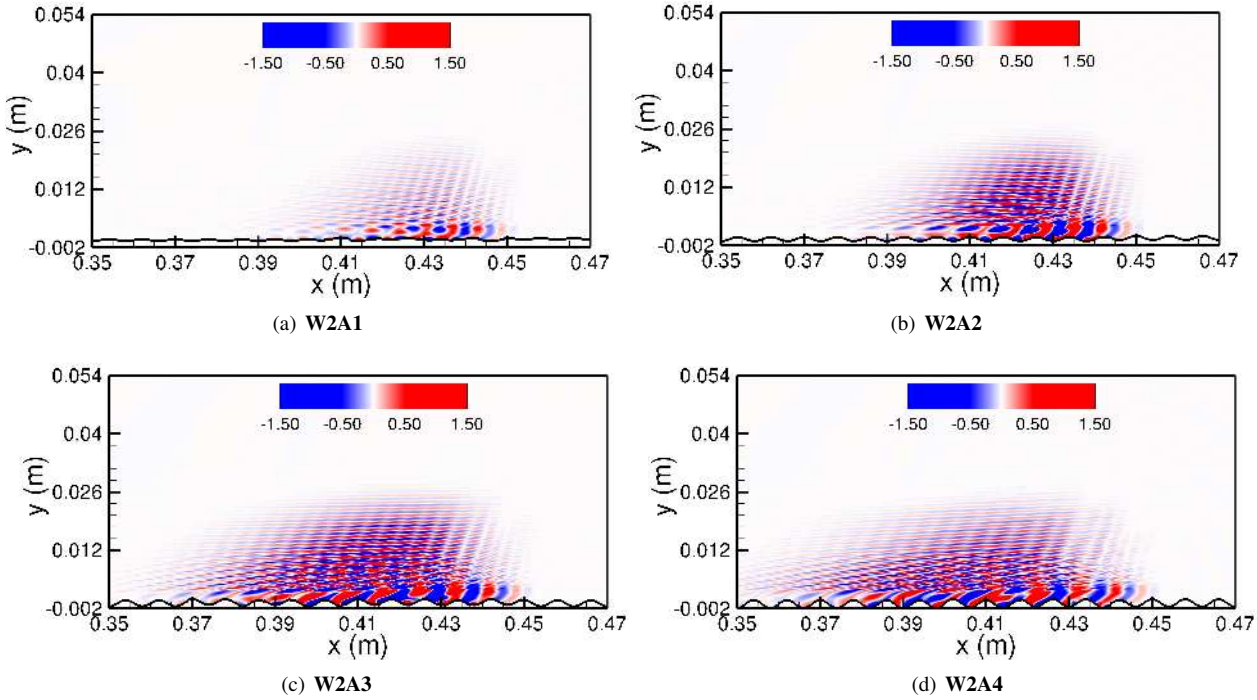

(a) **W2A1** (b) **W2A2**

(c) **W2A3** (d) **W2A4**

Fig. 6 Disturbance pressure flow field for the four wavy wall cases from Table 1.

smooth wall attains slightly higher temperature at $y = 0$ m compared to the amplitude varying cases.

B. Simulation of the disturbance flow field

Using the steady mean flow, next we computed the disturbance flow field corresponding to the amplitude varying cases and a snapshot of the disturbance pressure is shown in Fig. 6. Similar to the smooth wall case, a 100 kHz pulse is introduced through the same forcing location and it can be seen that near the wall, the disturbance structure is similar to the smooth flat plate case, where the second mode is the dominant instability (see Fig. 1(b)). Compared to the smooth wall case, all of the wavy wall cases show higher values of disturbance pressure. A plausible explanation for the pressure disturbances appearing on top of the second mode dominated wave packet is interactions of the wave packet with supersonic wave patterns of the baseflow generated by the rough surface. Because of this, disturbance pressure decays very slowly outside the boundary layer as compared to the smooth wall case. As the roughness height is increased, the interaction between the disturbances near the wall and the Mach waves becomes stronger, which leads to a more intense streaky structure. A further increase in the roughness height from 32.6% to 43.5% results in a slight reduction in the disturbance pressure at this location $x = [0.35 - 0.47]$ m as can be seen from comparing Fig. 6(d) with 6(c).

For a detailed analysis of the disturbance flow field, we have performed a fast Fourier transform (FFT) of the wall-pressure signal, and the amplitude distribution is presented in Fig. 7 as a function of stream wise location and frequency. For the wavy wall cases, the amplitude values are plotted after taking an average over each roughness wavelength throughout the domain. Comparing Fig. 7(b) with Fig. 7(a) we notice that introducing roughness at the flat plate surface, with a roughness height which corresponds to only 10.4% of the boundary layer thickness, slightly amplifies the disturbance amplitude and increases the region of disturbance growth in the frequency and x-plane. A further increase in the roughness amplitude to 21% enhances the high amplitude region significantly (see Fig. 7(c)), indicating a higher amplification of disturbance amplitude at the end of the domain. Increasing the roughness height to 32.6% leads to a significantly increase in the pressure amplitude, which is slightly reduced as the roughness height is further increased to 43.5%. It can also be observed that as the roughness height is increased, the high amplitude region shifted to lower disturbance frequencies, which suggests that the peak growth rate of the dominant second mode might shift to a lower frequency. Moreover, while the first region shifts to lower frequencies there seems to appear a second region at high frequencies. The second region becomes clearly visible when the roughness height is further increased to 32.6% (Fig. 7(d)) and 43.5% (Fig. 7(e)) of the boundary layer thickness.

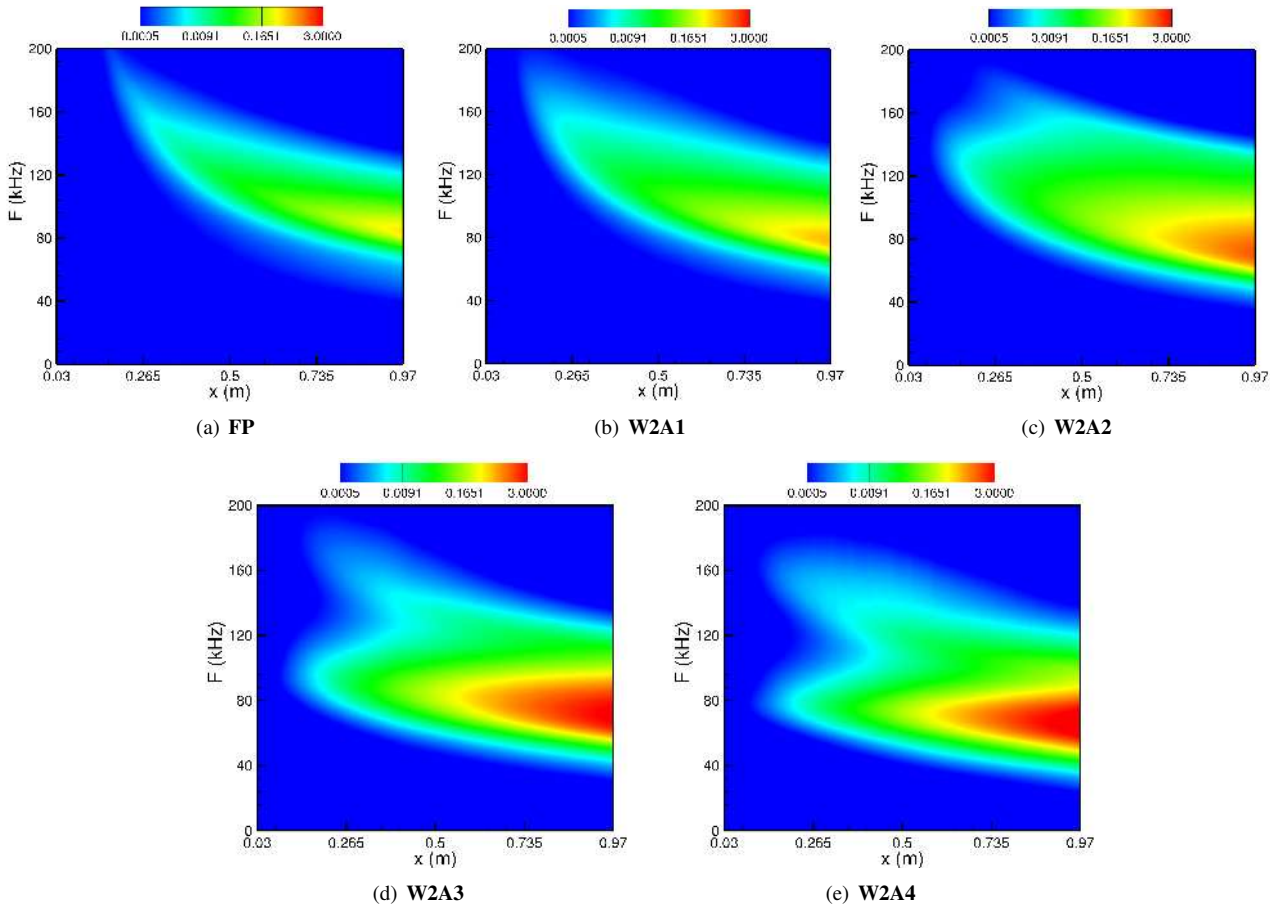

(a) **FP** (b) **W2A1** (c) **W2A2**

(d) **W2A3** (e) **W2A4**

Fig. 7 Contours of Fourier transformed disturbance pressure amplitude as a function of frequency and stream wise distance showing the effect of a change in the roughness amplitude.

To get a better understanding about the instability mechanisms and identify the unstable regions in frequency, we next computed the growth rate ($-\alpha_i = \frac{\partial}{\partial x}(\log|\tilde{P}_w|)$) based on the wall-pressure amplitude $|\tilde{P}_w|$ and plotted it in Fig. 8(a) at $x = 0.4$ m. The region above the black dashed line with $-\alpha_i > 0$ is the unstable region. The maximum amplification of the second mode corresponding to the smooth flat plate is observed at 116 kHz, whereas the presence of roughness at the wall reduces the growth rate of this mode at this location. As the roughness height is increased, the peak value of the second mode shifts to a lower disturbance frequency with a lower magnitude. However, the unstable region increases in frequency range since the second mode appears at a lower frequency and it is hypothesized that another instability mode appears at a higher frequency for the cases with roughness height greater than or equal to 21% of the boundary layer thickness as observed in Fig. 7. This additional mode that appears around 150 kHz for the **W2A2** case becomes more amplified and shifts to a lower disturbance frequency as the roughness amplitude is increased.

Figure 8(b) compares the amplification rates along the stream wise direction of the smooth plate with the amplitude varying wavy wall cases at frequencies corresponding to the peak growth rate of the second mode obtained from Fig. 8(a). Although the flat plate shows the highest amplification at $x = 0.4$ m corresponding to $F = 116$ kHz, the growth rate of the second mode drops significantly after attaining the maximum growth and becomes stable after $x = 0.54$ m. The lower amplitude roughness case also shows a similar trend and becomes stable slightly downstream ($x = 0.68$ m) of the smooth wall location. The effect of increasing the roughness height is clearly observed for the remaining three amplitude varying cases, where the maximum amplification rate is lower, however, the unstable region is longer leading to larger amplitudes at the end of the domain (see Fig. 7). The highest roughness case leads to the largest growth of the second mode at the end of the flat plate as can be observed from Fig. 8(b).

Next, the N-factor ($N = \log(A/A_o)$) curves are generated to gain more information about the amplification rates at

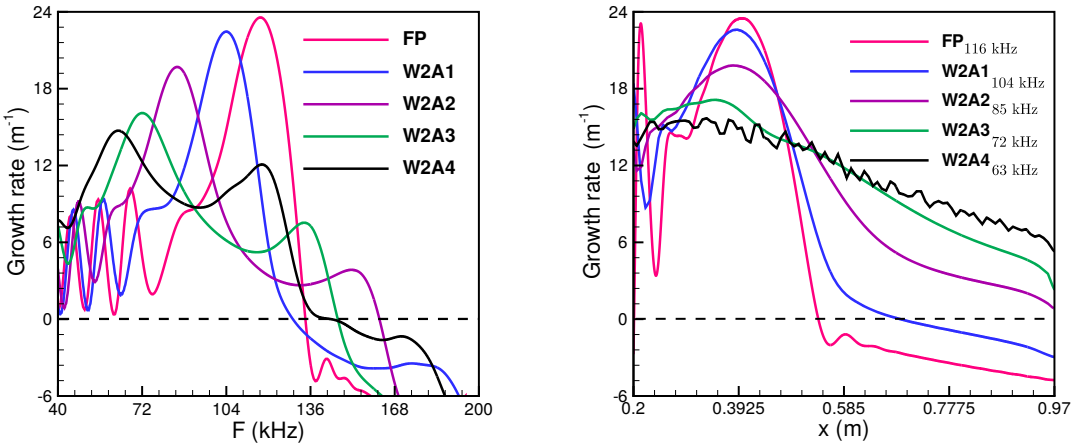

(a) Growth rate as a function of frequency

(b) Growth rate along the surface

Fig. 8 (a) Comparison of the averaged growth rate over a roughness wavelength centered at x=0.4 m for the four amplitude varying cases compared with the smooth wall data at varying frequencies. (b) Comparison of the growth rate plotted along the surface of the plate.

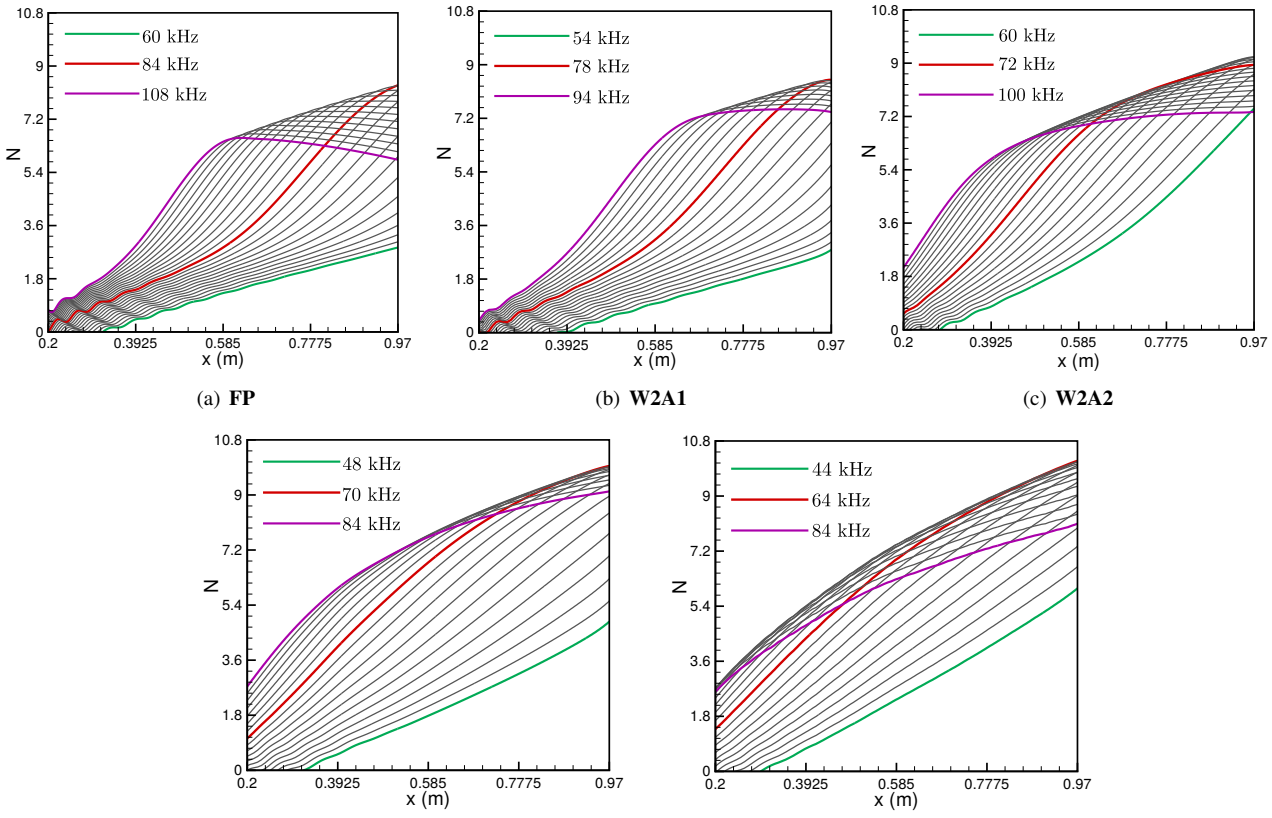

(a) **FP** (b) **W2A1** (c) **W2A2**

(d) **W2A3** (e) **W2A4**

Fig. 9 Effect of variation of roughness amplitude on the N-factor for a range of disturbance frequency plotted as a function of steam-wise distance with a step of 2 kHz. The red line indicating the frequency leading to the maximum N-factor at the end of the domain.

each downstream location for a wide range of frequencies with increments of ΔF = 2 kHz and plotted in Fig. 9. The green and purple lines denote the starting and the ending frequency, respectively, for each case. The red line corresponds to the disturbance frequency leading to the maximum N-factor at the end of the computational domain. A maximum N-factor of approximately 8.35 is reached at the end of the domain for the smooth flat plate (see Fig. 9(a)), whereas the smallest roughness amplitude case **W2A1** shown in Fig. 9(b) leads to a slightly higher N-factor of 8.5 at the same location. The frequency corresponding to the maximum N-factor reduces from 84 kHz for the smooth wall case to 78 kHz for the wavy wall case. Increasing the roughness height to 21% increases the maximum N-factor to around 9.22, corresponding to a disturbance frequency of 72 kHz. The remaining two larger roughness amplitude cases **W2A3** and **W2A4** cause more amplification of the initial disturbance amplitude A_o and lead to N-factor values of 9.97 and 10.68 at the end of the plate, respectively corresponding to a frequency of 70 kHz and 64 kHz. Therefore, the addition of distributed roughness of a small height which is around 10% of the boundary layer thickness can also destabilize the flow in comparison to a smooth wall case at the same conditions. This is an interesting finding since previous works have reported that large roughness heights are required to affect the transition process. Also, compared to a smooth flat plate, the wavy geometry with higher roughness amplitudes will lead to transition at a much lower disturbance frequency, as can be seen from Figs. 9(d) and 9(e). A detailed discussion on the energy transfer mechanisms leading to the amplification of disturbances is provided in the next subsection.

C. Energy analysis for the wavy wall cases with varying roughness height

To gain further insight into the physical mechanisms causing the disturbances to amplify or decay, we derived an energy balance equation based on the linear disturbance equations (2). The total energy transfer equation (4) is obtained by multiplying the x-momentum (6), y-momentum (7), energy equation (8), and the continuity equation (9) by the coefficients of the Chu's energy norm [25], which are $\tilde{u}$, $\tilde{v}$, $\tilde{T}/\bar{T}$, and $(R\bar{T}\tilde{\rho})/\bar{\rho}$, respectively.

$$\begin{aligned} \mathrm{TE} &= \bar{u}\frac{\partial \tilde{E}}{\partial x} + \bar{v}\frac{\partial \tilde{E}}{\partial y} = \mathrm{P_{tot}} + \mathrm{D_{tot}} + \mathrm{F_{tot}}; \\ \tilde{E} &= 0.5\Big(\frac{\bar{P}}{\bar{\rho}^2}\tilde{\rho}\tilde{\rho}^* + \bar{\rho}\tilde{u}_i\tilde{u}_i^* + \frac{\bar{\rho}R}{(\gamma-1)\bar{T}}\tilde{T}\tilde{T}^*\Big). \end{aligned} \tag{4}$$

Here, $\tilde{E}$ represents the total energy contained in the disturbance. The rate of change of total disturbance energy TE is decomposed into the total production term $\mathrm{P_{tot}}$, total dissipation term $\mathrm{D_{tot}}$, and the total flux term $\mathrm{F_{tot}}$. Each of these terms contain the following components:

$$\begin{aligned} \mathrm{P_{tot}} &= \mathrm{P_{RS}} + \mathrm{P_{Mom}} + \mathrm{P_{Entropy}} + \mathrm{P_{PW}} + \mathrm{P_{Conv}} + \mathrm{P_{Dila}} + \mathrm{P_{IE}} + \mathrm{P_{TP}}; \\ \mathrm{D_{tot}} &= \mathrm{D_{Cond}} + \mathrm{D_{SW}}; \\ \mathrm{F_{tot}} &= \mathrm{F_{TP}} + \mathrm{F_{HF}} + \mathrm{F_{PW}} + \mathrm{F_{SW}}. \end{aligned}$$

The total production term $\mathrm{P_{tot}}$ consists of the contributions from the Reynolds stress $\mathrm{P_{RS}}$, convective stress $\mathrm{P_{Conv}}$, momentum stress $\mathrm{P_{Mom}}$ due to the convection of the disturbance momentum, entropy stress $\mathrm{P_{Entropy}}$ because of entropy spottiness, stress related to pressure work $\mathrm{P_{PW}}$, and the stress generated due to the non-zero divergence field $\mathrm{P_{Dila}}$. In addition, the variation of transport properties gives rise to the production term $\mathrm{P_{TP}}$, and the spatial variation of the internal energy leads to the production term $\mathrm{P_{IE}}$. The total dissipation term mainly consists of two terms i.e., shear-work generated dissipation $\mathrm{D_{SW}}$, and the heat-flux related term $\mathrm{D_{Cond}}$. The flux terms redistribute energy throughout the domain and they are considered as a volume contribution in this work. $\mathrm{F_{PW}}$ and $\mathrm{F_{SW}}$ correspond to the flux generated due to pressure work and shear work, respectively, whereas the flux arising due to transport property variation and heat transfer are denoted by $\mathrm{F_{TP}}$ and $\mathrm{F_{HF}}$, respectively. A detailed description of these terms is provided in Appendix A.

To calculate the energy budget terms, we simulated the disturbance flow field by using a continuous time-periodic volume forcing. The volume forcing term is added to the right-hand side of the y-momentum equation (Eq. (7)). This will impose only a single frequency, and the frequency is selected such that that it leads to the maximum amplification of the second mode, which was determined from the previous pulse simulations. The forcing function can be expressed as,

$$G(x,y,t) = A\sin\Big(\frac{2\pi(\mathrm{x}-\mathrm{x_s})}{\Delta \mathrm{x_w}}\Big)\exp\Big(-\frac{(\mathrm{y}-\mathrm{y_o})^2}{\sigma_\mathrm{f}^2}\Big)\sin(2\pi \mathrm{Ft}); \tag{5}$$

$\Delta x_w = x_e - x_s$ is the width of the forcing slot and the disturbance is introduced at y_o in the wall-normal direction. The imposed frequency is F and σ_f is the standard deviation of the distribution.

The total energy transfer term from Eq. (4) is presented in Fig. 10 after averaging over one forcing period, which corresponds to the frequency leading to the maximum second mode growth in Fig. 8(a) at $x = 0.4$ m. For the wavy wall cases, the energy transfer terms are also averaged over the roughness wavelength between $x = [0.396 - 0.404]$ m. All the energy transfer terms plotted in this work are normalized by $\int_{y=0}^{y=0.04} 2\bar{u}\tilde{E}dy$, which is proportional to the term $\bar{u}\frac{\partial \tilde{E}}{\partial x}$, that appears on the LHS of the total energy transfer equation (4). The inset in the figure shows that close to the wall and until the critical layer, the disturbance gains more energy in the smooth flat plate case in comparison to the rough wall cases. It can also be observed that as the height of the roughness elements increases, the disturbances loose energy at a faster rate away from the wall. The smooth flat plate shows the highest peak in the TE term in the critical layer. The first peak in TE increases as the roughness height is increased, however, as the roughness height reaches around 43% of the boundary layer thickness, the peak value reduces. The second peak is largest for the smallest roughness case **W2A1**, compensating the reduction in the first peak and leading to the largest amplification of the second mode among the wavy wall cases at $x = 0.4$ m. The presence of large fluctuations of energy is noticed outside the boundary layer for the wavy wall cases. The integrated value of TE along the boundary layer reduces as the roughness height is increased which explains the lower amplification rate of the second mode observed in Fig. 8 at $x = 0.4$ m with increasing roughness amplitude.

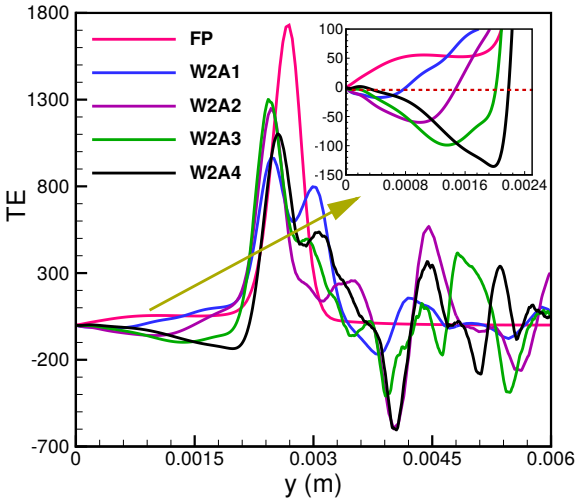

Fig. 10 Effect of variation of roughness amplitude on the total energy transfer rate plotted as a function of the wall-normal direction at x=0.4 m.

V. Effects of variation of roughness wavelength

This wavy-wall stabilization (WWS) concept suggests replacing the long separation bubbles with a sequence of small ones to avoid any detrimental acoustic resonances within the bubbles. It is believed that the second mode is damped due to the stabilizing effect of a relatively long free shear layer formed near a streamlined surface [26]. This concept was verified by the numerical investigation of Zhou et al. [15], which showed that a wavy wall with multiple wavenumbers can suppress the second-mode growth significantly as compared to a wavy wall with a single wave number. This was attributed to the multiple separation regions as opposed to a shorter re-circulation region corresponding to a single roughness element. This highlights the stabilizing role of distributed roughness compared to an isolated roughness element. The importance of the size of the roughness wavelength was demonstrated by Fujii [20], which conducted an experimental investigation on a 5 degree half-angle sharp cone at Mach 7.1. His work showed that a wavy wall with a wavelength of twice the boundary layer thickness located well upstream of the breakdown region can delay the transition process. In this section, we will review the wavy-wall stabilization concept using sinusoidal roughness elements with shorter to longer wavelengths scaled as a function of the second mode wavelength with a fixed roughness height which is around 21% of the boundary layer thickness corresponding to a smooth flat plate at $x = 1$ m.

A. Effect of varying roughness wavelength on mean flow field

To analyze the effect of a change in the roughness wavelength on the mean flow, we have constructed four test cases which are listed in Table 2. The steady mean flow fields corresponding to these wavelength varying cases are presented in Fig. 11 in terms of pressure contours. The stream wise domain shown in the figure includes two roughness wavelengths corresponding to the highest wavelength case **W4A2**. Similar to the amplitude varying cases discussed in the previous section, the roughness elements start at $x = 0.026$ m, where the first expansion fan is observed, marked by the dark black pressure contours. The flow fields appear similar to the amplitude varying wavy wall cases presented in Fig. 3 in terms of the expansion and compression waves generated at the surface. The main effect of increasing the roughness wavelength is to increase the strength of expansion and compression waves generated by the roughness elements. This can be visualized from a change of contour colors from light yellow in Fig. 11(a) for the smallest roughness wavelength case to a dark red color in Fig. 11(d) corresponding to the largest wavelength case. A comparison of the mean flow pressure extracted at $y = 0$ m for all four cases is shown in Fig.11(e) along with the smooth wall data.

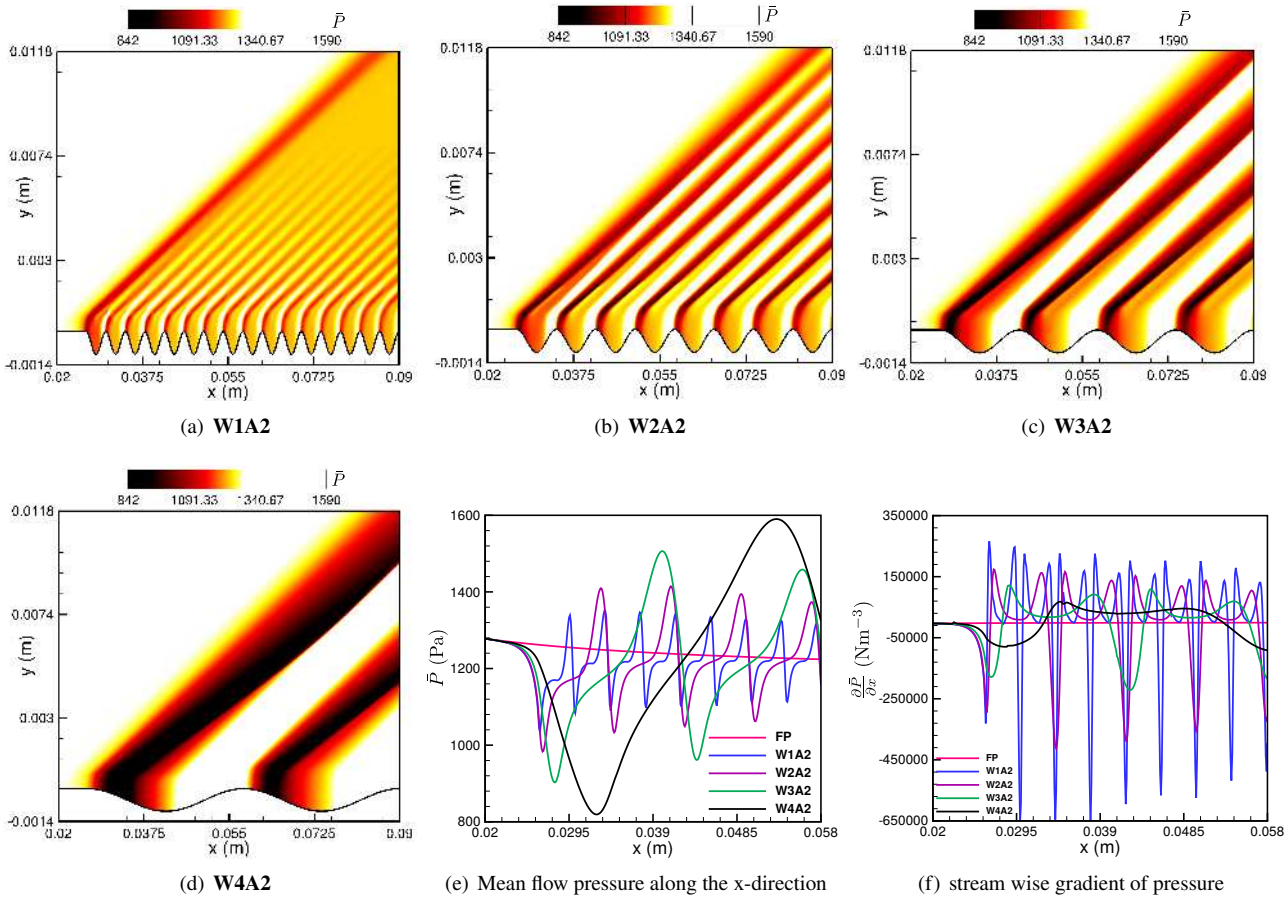

(a) **W1A2** (b) **W2A2** (c) **W3A2**

(d) **W4A2** (e) Mean flow pressure along the x-direction (f) stream wise gradient of pressure

Fig. 11 (a)-(d) Contours of pressure showing the effect of varying the roughness wavelength on the mean flow field. Variation of (e) mean flow pressure and (f) its stream wise gradient above the first roughness element corresponding to the largest wavelength case W4A2 extracted at y=0 m.

Compared to the smooth flat plate case, all the wavy wall cases cause large variations in the mean flow quantities, which becomes more severe when the roughness wavelength is increased. The plot of stream wise pressure gradient along the surface of the plate in Fig. 11(f) indicates that the smallest wavelength case **W1A2** leads to the largest pressure gradients. The d-type behavior can be noticed for all the wavelength varying cases except the largest case **W4A2** (see Fig. 12(d)). Increasing the roughness wavelength causes a smoother change of pressure gradient with a reduced magnitude, which can be clearly seen for the largest wavelength case **W4A2** in Fig. 11(f), leading to a smaller separation bubble (see Fig. 12(d)). This also causes the shear layer to bend inwards, moving closer to the wall, as opposed to a parallel shear layer corresponding to the smaller wavelength cases, where the shear layer smoothly connects the crests of the neighboring roughness elements.

The variation of stream wise velocity and temperature is plotted along the boundary layer in Fig. 13 after averaging over a roughness wavelength centered at $x = 0.4$ m for the wavy-wall cases. Although all the rough wall cases in Fig. 12 show separation, it is not evident from the velocity profiles presented in Fig. 13(a). This is because the profiles are extracted above the separation bubble, starting from $y = 0$ m to keep the lower bound the same as the smooth plate surface. As the roughness wavelength is increased, $\bar{u}$ attains a higher value at $y = 0$ m. The smallest roughness wavelength case **W1A2** quickly follows the smooth wall data away from the wall, however, the other three cases align with the smooth wall data only at the boundary layer edge. All the wavelength varying cases except the smallest wavelength case lead to a lower temperature in the boundary layer compared to the smooth wall data (see Fig. 13(b)). The highest temperature is observed at the flat plate surface due to imposed adiabatic boundary conditions. Although the **W1A2** case attains a lower temperature at $y = 0$ m compared to the smooth flat plate case, it shows a slightly higher temperature away from the wall and leads to a slightly higher thermal boundary layer thickness compared to the other

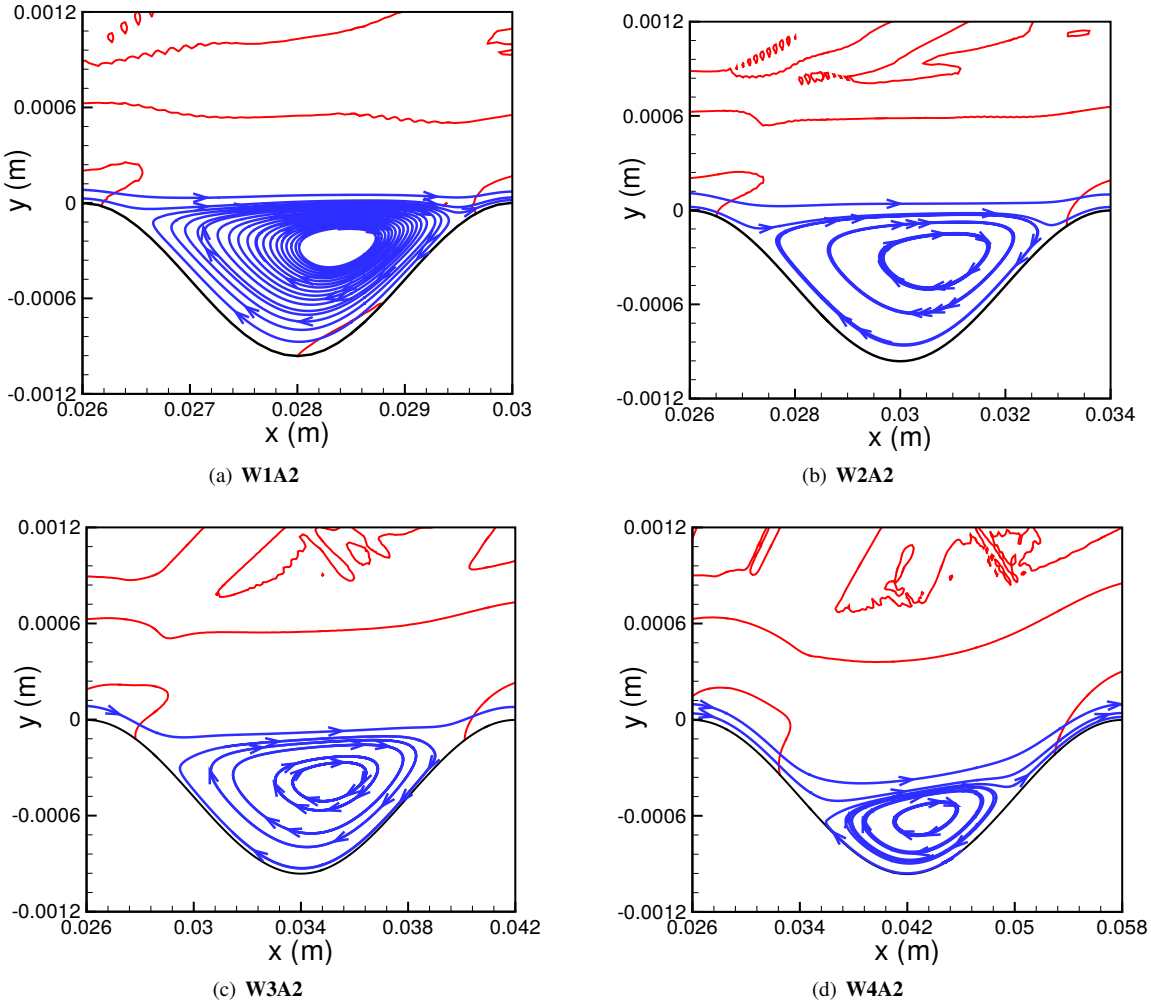

(a) **W1A2** (b) **W2A2**

(c) **W3A2** (d) **W4A2**

Fig. 12 Zero contours of inflectional profile $\frac{\partial}{\partial y}(\bar{\rho}\frac{\partial \bar{u}}{\partial y})$ demonstrating the regions of separated flow over a roughness wavelength for the four wavelength varying cases from Table 2.

cases.

B. Effects of varying roughness wavelength on disturbance flow field

Using the steady base flows presented in the previous section, next we computed the disturbance flow fields for the wavelength varying cases by introducing a 100 kHz pulse as discussed in Section III. To visualize the disturbance flow field, we have plotted the pressure contours corresponding to each of these cases from Table 2 in Fig. 14. Since the contour legend is kept at the same range as that of the smooth flat plate case presented in Fig. 1(b), the wavy wall with half of the second mode wavelength seem to slightly reduce the disturbance pressure values, with a shorter wave packet (see Fig. 14(a)). The interaction of the second mode disturbance with the Mach waves does not lead to any amplification of the disturbance amplitude in this case. When the roughness wavelength approaches the second mode wavelength, an intense amplification of the pressure amplitude is observed as can be seen from Fig. 14(b). A resonance mechanism might be set up when both the wavelengths are of the same order, causing the growth of disturbance quantities. The streaky structures created on top of the roughness elements also intensify. Increasing the roughness wavelength to around twice the second mode wavelength causes a slight reduction in the pressure amplitude, however, the interaction between the second mode and the Mach waves extends to a broader region in the wall-normal direction (see Fig. 14(c)). A further increase in the roughness wavelength causes less interaction of the near-wall disturbances with the Mach

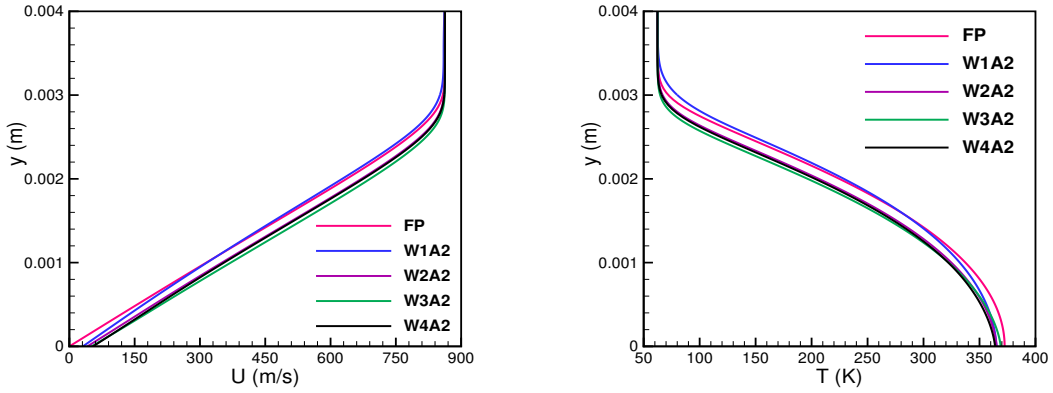

(a) stream wise velocity

(b) Temperature

Fig. 13 Comparison of (a) velocity and (b) temperature profiles averaged over a roughness wavelength for the four wavelength varying cases compared with the smooth wall data extracted at x=0.4 m.

waves, leading to a significant reduction in the streaky structure and the pressure amplitude away from the wall. As the roughness wavelength is increased further, the stability characteristics will behave similarly to a smooth flat plate geometry. This is expected since the surface of the smooth flat plate can be assumed as a single roughness element with a wavelength of the infinite radius of curvature.

To determine the range of frequencies leading to the maximum growth of near-wall disturbances for the wavelength varying cases, we performed a fast Fourier transform of the wall-pressure data. The FFT pressure amplitude obtained after averaging over each roughness wavelength is plotted in Fig. 15 as a function of frequency and stream wise distance. Compared to the smooth wall case shown in Fig. 15(a), the lowest wavelength case shifts the large amplitude region downstream and also to a lower disturbance frequency (see Fig. 15(b)). A comparison of the two cases is shown as a function of frequency in Fig. 16(a) after extracting the pressure amplitude at $x = 0.4$ m. The wavy wall case **W1A2** has a much lower amplitude than the smooth wall case as can be seen from the figure. It also shows a much earlier amplification of the disturbance starting from around 30 kHz and leads to a broader peak in pressure amplitude spanning between $30 - 150$ kHz. Compared to **W1A2** case, the smooth flat plate causes a delayed amplification of pressure (≈ 98 kHz) and the peak value appears around 130 kHz. The amplitude data plotted at the end of the domain in Fig. 16(b) shows a large increase in the pressure amplitude and the smallest wavelength case attains a comparable amplitude as that of the smooth wall data, however at a much lower frequency. Increasing the roughness wavelength from $\lambda = 0.004$ m to 0.008 m enhances the pressure amplitude significantly as can be seen from Fig. 15(c). It also leads to a shift in the amplitude loop to a lower stream wise location, while including a wider range of disturbance frequencies. At $x = 0.4$ m, the **W2A2** case which has a comparable roughness wavelength as that of the second mode leads to the highest increase in the pressure amplitude. However, the wavy-wall case **W3A2** with $\lambda = 0.016$ m leads to the maximum amplitude growth at the end of the domain (see Fig. 16(b)). The variation of pressure in Fig. 16(a) indicates that there might be another instability mode around 132 kHz in addition to the second mode appearing at 102 kHz for the wavy wall case **W3A2**. As the roughness wavelength is increased further, the second peak in pressure attains a slightly higher magnitude compared to the first peak at $x = 0.4$ m, however, both the peaks have a much smaller amplitude than the two wavy wall cases **W2A2** and **W3A2**, but still higher than the smooth wall data. This highest wavelength case **W4A2** attains a similar magnitude of pressure as that of the **W2A2** case at the end of the wavy surface (see Fig. 16(b)), with the first peak having a higher amplitude than the second one. It can be observed that at both the x-locations, the first peak in pressure appears at a much lower disturbance frequency for the four wavelength varying cases compared to the smooth wall case.

Next, we computed the amplification rates based on the averaged wall pressure amplitude to identify the unstable regions along the plate at varying frequencies. The growth rate extracted at $x = 0.4$ m is plotted in Fig. 17 as a function of disturbance frequency. Among all the cases, the smooth flat plate leads to the largest growth of the second mode at this x-location. As observed in Fig. 16(a), the unstable region is shifted to a higher frequency range compared to the four wavelength varying cases, with the peak growth rate appearing at $F = 116$ kHz. The smallest wavelength case **W1A2** shows the smallest amplification of the second mode and the unstable region covers a frequency range between

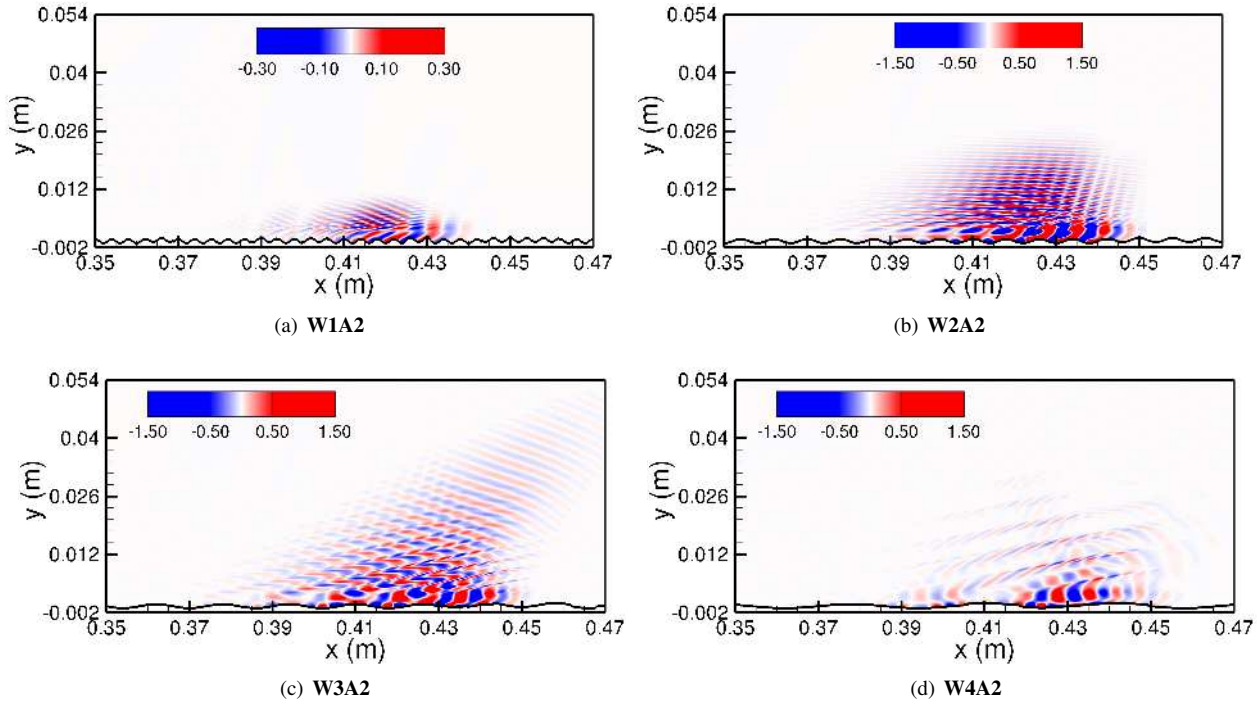

(a) **W1A2** (b) **W2A2**

(c) **W3A2** (d) **W4A2**

Fig. 14 Effect of variation of roughness wavelength on the disturbance pressure flow field for the four wavy wall cases from Table 2.

50 – 118 kHz. The lowest amplification corresponding to this case is expected since it has the largest thermal boundary layer thickness (see Fig. 13(b)). Increasing the roughness wavelength to 0.008 m causes a significant increase in the growth rate, with the peak value shifted to a slightly higher frequency compared to the lowest wavelength case. This case **W2A2** is unstable over all the frequency range considered in this plot. A slight reduction in the amplification rate is noticed at $x = 0.4$ m as the roughness wavelength is increased further to 0.016 m. The frequency corresponding to the maximum second mode growth is shifted further to 89 kHz compared to the previous two-wavelength varying cases. As observed in the FFT diagram in Fig. 15(d), another unstable mode is observed around 129 kHz for the **W3A2** case. Although the frequency corresponding to the peak second mode growth is shifted slightly to a lower value, the highest wavelength case **W4A2** leads to a similar amplification of the second mode as that of the wavy-wall case **W2A2**. However, it also shows two other instability peaks at higher frequencies, which is not observed in the **W2A2** case. The frequency corresponding to the second peak observed in the **W4A2** case is shifted to a lower value compared to the **W3A2** case, but with a higher magnitude. Similar to the effect of increasing roughness height observed in Fig. 8, multiple instability modes appear in the flow field as the roughness wavelength is increased and the higher modes move to a lower disturbance frequency with an increase in the roughness wavelength.

To identify the unstable regions above the plate, we plotted the amplification rates at frequencies corresponding to the peak growth rate of the second mode at $x = 0.4$ m in Fig. 17(b). Although the smooth flat plate becomes stable after $x = 0.53$ m, all the wavelength varying cases are unstable throughout the entire computational domain. After attaining the maximum growth rate at $x = 0.4$ m, all the wavy wall cases except the largest wavelength case show a gradual decrease in the disturbance growth. The wavy wall case **W4A2** shows another peak in growth rate around $x = 0.8$ m corresponding to a frequency of 83 kHz. Based on these growth rates, we next computed the N factors at multiple frequencies to determine how much disturbance has amplified over the computational domain. Compared to the N-factor of 8.35 for the smooth flat plate, the lowest wavelength case **W1A2** leads to a slightly lower N-factor (= 7.9) at the end of the domain. The red line in Fig. 18 corresponds to the frequency leading to the maximum N-factor at the end of the plate. Adding a small roughness wavelength $\lambda = 0.004$ m to the surface of the flat plate reduces this frequency from 84 kHz in the smooth wall case to 66 kHz in the **W1A2** case, which can be seen by comparing Fig. 18(b) with 18(a). When the roughness wavelength approaches the second mode wavelength, a significant increase in the N-factor (= 9.22) is observed at $x = 0.97$ m compared to the smallest roughness case. Figure 18(c) shows that frequency corresponding

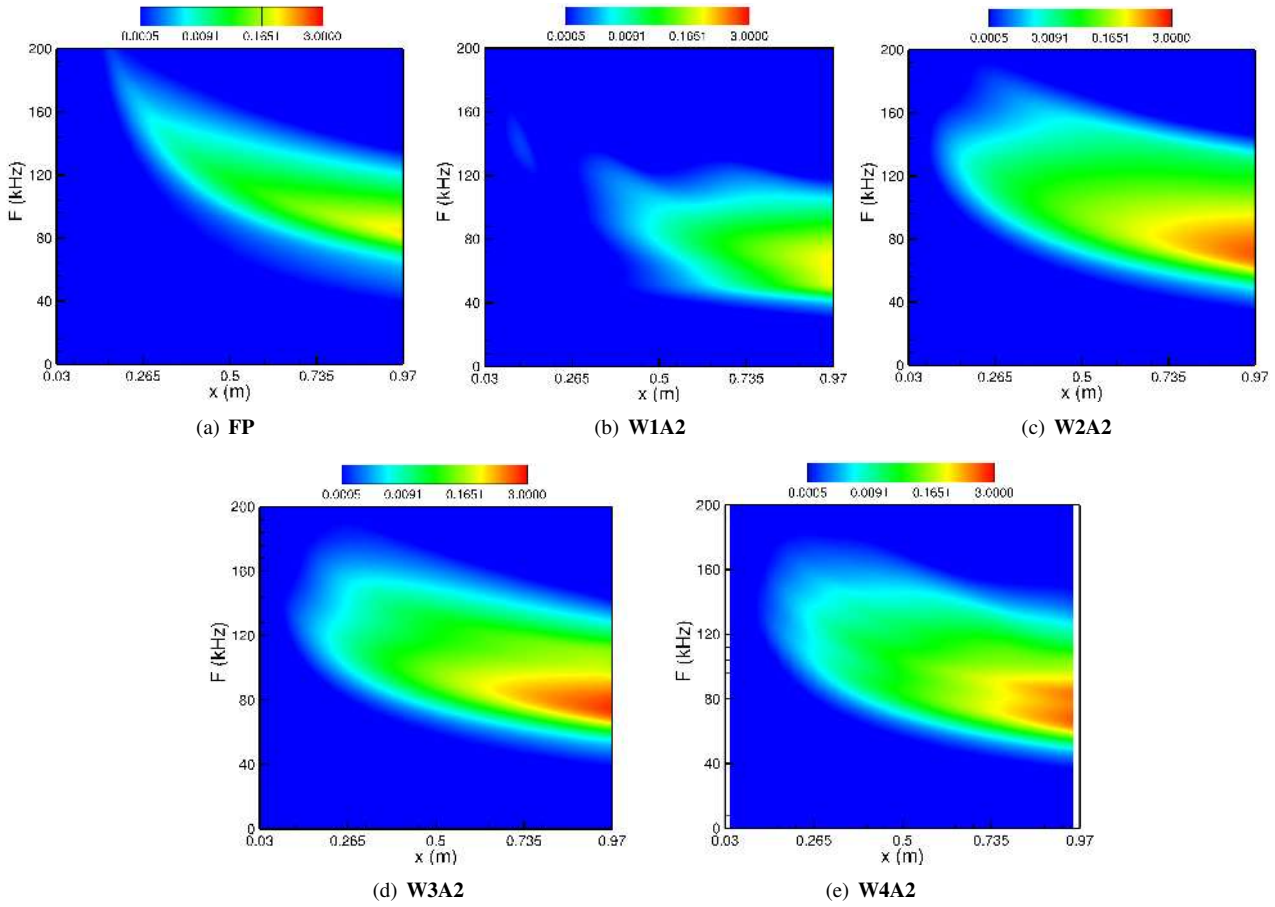

(a) **FP** (b) **W1A2** (c) **W2A2**

(d) **W3A2** (e) **W4A2**

Fig. 15 Fourier transformed disturbance pressure amplitude for different roughness wavelength cases.

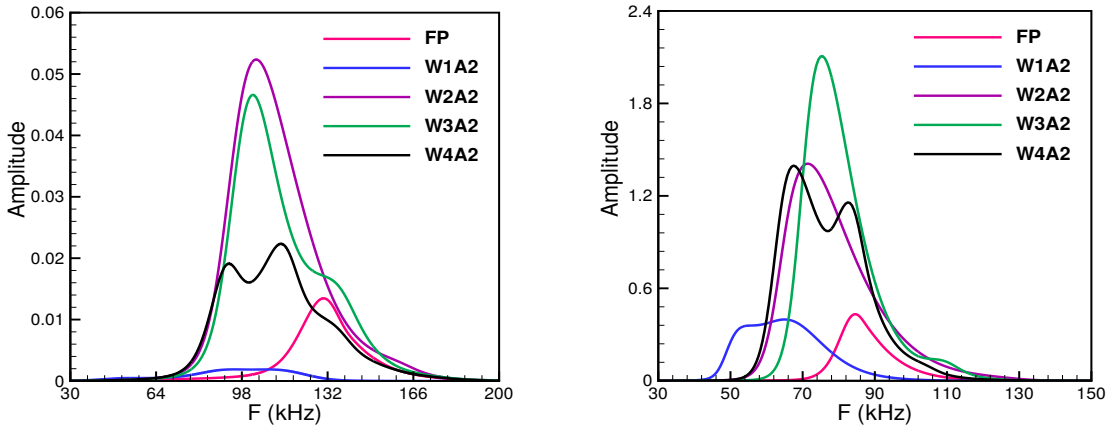

(a) Averaged amplitude as a function of frequency (b) Averaged amplitude as a function of frequency

Fig. 16 Comparison of the averaged pressure amplitude extracted at (a) x=0.4 m and (b) x=0.97 m plotted as a function of disturbance frequency.

to the maximum N-factor for this case 72 kHz. Increasing the roughness wavelength further increases the maximum N-factor value to 10.1 corresponding to a disturbance frequency of 76 kHz for the **W3A2** case (see Fig. 18(d)). The

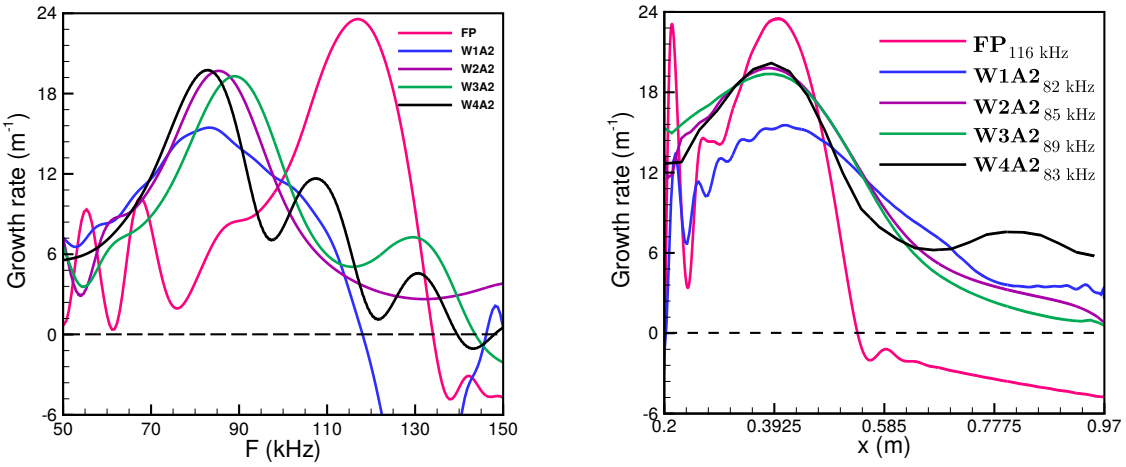

(a) Growth rate as a function of frequency

(b) Growth rate along the surface

Fig. 17 Comparison of the averaged growth rate (a) over a roughness wavelength centered at x=0.4 m for the four wavelength varying cases compared with the smooth flat plate case as a function of frequency and (b) along the wall corresponding to the frequencies leading to the maximum second mode growth rate in (a).

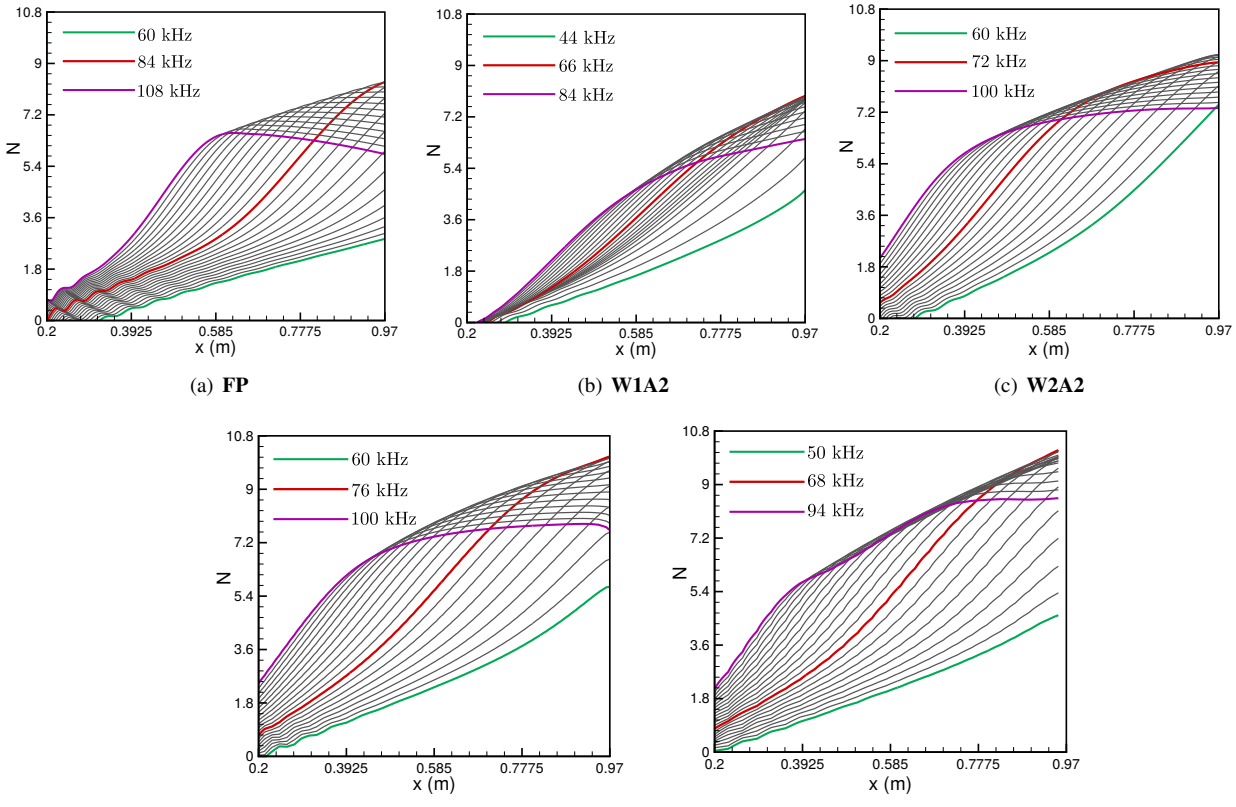

(a) **FP** (b) **W1A2** (c) **W2A2**

(d) **W3A2** (e) **W4A2**

Fig. 18 Effect of variation of roughness wavelength on the N-factor for a range of disturbance frequency plotted as a function of steam-wise distance with a step of 2 kHz. The red line indicating the frequency leading to the maximum N-factor at the end of the domain.

largest wavelength case **W4A2** amplifies the disturbances slightly more than the **W3A2** case, with the N-factor reaching a value of 10.14 at a much lower frequency of 68 kHz. Therefore, shorter wavelength roughness elements can delay the transition process compared to a smooth flat plate. However, increasing the roughness wavelength can lead to transition faster and at a much lower disturbance frequency than the smooth wall case.

Next, to conduct an energy analysis of the disturbance flow, we computed the disturbance flow fields for the wavelength varying cases by using continuous forcing at forcing frequencies leading to the maximum second mode growth at $x = 0.4$ m shown in Fig. 17. The energy budget terms provided in Eq. 4 are calculated after averaging over one period of the disturbance corresponding to each of these frequencies. The terms are also averaged over one roughness wavelength centered at $x = 0.4$ m and normalized by the $\int_{y=0}^{y=0.04} 2\bar{u}\tilde{E}\,dy$ term. A comparison of the total energy transfer term in Eq. (4) is shown in Fig. 19 as a function of the wall-normal distance. A close-up view of the near-wall variation of TE is shown in the inset. It shows that, in the near wall region, the disturbance flow field gains the largest amount of energy for the smooth wall case, whereas two shortest wavelength cases **W1A2** and **W2A2** dissipate disturbance energy until the critical layer. The amount of energy lost near the wall is reduced as the roughness wavelength is increased further. Although disturbance flow field gains energy at the two extrema of the shear layer, energy is also dissipated around $y = 0.003$ m inside the shear layer for the shortest roughness case **W1A2**. The integrated value of TE along the boundary layer is smallest for this case among all the cases presented in Fig. 19. Therefore, the smallest wavelength case **W1A2** shows the lowest amplification of the second mode compared to the other wavelength varying cases. The highest growth rate is observed for the smooth wall case at $x = 0.4$ m in Fig. 17 and it can be attributed to the largest peak in TE as well as the larger energy transfer in the near-wall region as can be seen from Fig. 19. Among the wavy wall cases, the highest peak in TE is observed for the **W2A2** case, making it more unstable than the higher wavelength case **W3A2**. Although the peak value of TE is lower in the largest wavelength case **W4A2**, the energy is transferred over a wider region in the boundary layer, making this case as unstable as the **W2A2** case (see Fig. 17).

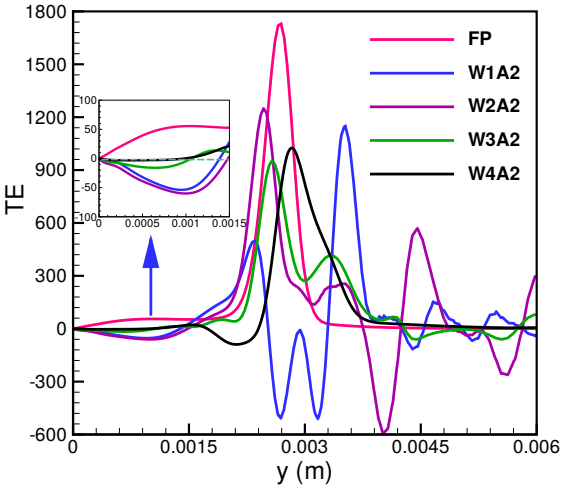

Fig. 19 Effect of variation of roughness wavelength on the total energy transfer term plotted as a function of the wall-normal direction at x=0.4 m, normalized by $\int_{y=0}^{y=0.04} 2\bar{u}\tilde{E}\,dy$.

VI. Conclusion

The stability of a high-speed boundary layer flow over smooth and rough surfaces was investigated using numerical simulations. A well-defined study was performed to isolate the effects of roughness wavelength and height. The test cases to investigate the effects of roughness height used roughness heights between 10 and 44 percent of the boundary layer height measured at the end of a 1 m long smooth flat plate. The wavelength varying cases were chosen to be between 0.44 and 3.55 of the second mode wavelength. For all roughness cases, a strong effect on the pressure field was noted with a supersonic wave pattern emanating away from the rough surface. Increasing the roughness height and roughness wavelength enhances the strength of these wave patterns that interact with the disturbance flow field. For all but the largest wavelength case, the separation regions filled essentially the entire cavities between consecutive roughness elements.

The disturbance flow field was obtained by solving the linear disturbance flow equations. A pulse disturbance centered around a frequency of around 100 kHz was introduced in the smooth wall section ahead of the roughness elements to generate a second mode dominated wave-packet. The disturbance flow field for the wavy wall cases looked similar near the wall to the smooth wall flat plate case displaying a typical two-cell structure representing the second mode. However, away from the wall, the interaction between the second mode dominated wave-packet and the waves emanating from the rough surface generated acoustic-like disturbances in the freestream. When the roughness wavelength was comparable to the second mode wavelength and the roughness heights were greater than or equal to 20% of the boundary layer thickness the interaction appears to be enhanced. The stability of the flow was investigated

by considering the Fourier transformed wall pressure signal and energy budget transfer term. For the cases with a fixed roughness wavelength, a destabilization of the flow was noticed for all roughness heights. However, for the shortest roughness wavelength case considered as part of the fixed roughness height cases a weak stabilization of the flow to second mode disturbances could be noticed. All distributed roughness cases with a wavelength comparable to the second mode wavelength or higher showed a destabilization of the flow. For all roughness cases, the frequency range where the disturbance flow field displayed the largest amplification shifted to lower frequencies in comparison to the smooth wall case.

Lastly, the energy budget transfer terms were computed to obtain some insight about the energy transfer mechanisms from the mean flow to the disturbance flow field. The plot of the total energy transfer terms looked very similar for the smooth and rough wall cases, where most of the energy transfer occurred close to the boundary layer edge. The main peak in the total energy transfer term was reduced for all roughness cases in comparison to the smooth wall and additional peaks appeared in the distributions for the roughness cases. For the wavy wall cases with larger roughness height, a significant amount of energy transfer is also observed outside the boundary layer due to the strong interaction between the disturbance flow field with the wave pattern generated by the rough surface. In general, the integrated value of the total energy transfer term for the roughness cases was lower than for the smooth wall case suggesting a lower amplification rate. However, the unstable flow region for the roughness cases was enlarged for most of the roughness cases which then led to larger overall N-factors at the end of the computational domain.

Acknowledgments

The authors would like to recognize and show appreciation for the financial support provided by NASA Kentucky EPSCoR RA Award no. 80NSSC19M0144 with E. Stern as the technical monitor and NASA EPSCoR R3 Award no. 80NSSC19M0084 with M. Bernhardt as the technical monitor. The authors would also like to thank the collaborators from NASA Ames Research Center, NASA Langley Research Center, and the NASA Johnson Space Center.

Appendix A

The x-momentum (6), y-momentum (7), energy equation (8), and the continuity equation (9) for the disturbance flow are mentioned below.

$$\begin{aligned}
&\bar{\rho}\left(\frac{\partial\tilde{u}}{\partial t}+\bar{u}\frac{\partial\tilde{u}}{\partial x}+\tilde{u}\frac{\partial\bar{u}}{\partial x}+\bar{v}\frac{\partial\tilde{u}}{\partial y}+\tilde{v}\frac{\partial\bar{u}}{\partial y}\right)+\tilde{\rho}\left(\bar{u}\frac{\partial\bar{u}}{\partial x}+\bar{u}\frac{\partial\tilde{u}}{\partial x}+\bar{v}\frac{\partial\bar{u}}{\partial y}+\bar{v}\frac{\partial\tilde{u}}{\partial y}+\tilde{u}\frac{\partial\bar{u}}{\partial x}+\tilde{v}\frac{\partial\bar{u}}{\partial y}\right)+\frac{\partial\tilde{p}}{\partial x}\\
&-\bar{\mu}\left(2\frac{\partial^2\tilde{u}}{\partial x^2}+\frac{\partial^2\tilde{u}}{\partial y^2}+\frac{\partial^2\tilde{v}}{\partial x\partial y}\right)-\bar{\lambda}\left(\frac{\partial^2\tilde{u}}{\partial x^2}+\frac{\partial^2\tilde{v}}{\partial x\partial y}\right)-\frac{\mathrm{d}\bar{\mu}}{\mathrm{d}\bar{T}}\left[2\left(\frac{\partial\tilde{u}}{\partial x}\frac{\partial\bar{T}}{\partial x}+\frac{\partial\tilde{T}}{\partial x}\frac{\partial\bar{u}}{\partial x}\right)+\tilde{T}\left(2\frac{\partial^2\bar{u}}{\partial x^2}+\frac{\partial^2\bar{u}}{\partial y^2}+\frac{\partial^2\bar{v}}{\partial x\partial y}\right)\right]\\
&-\frac{\mathrm{d}\bar{\mu}}{\mathrm{d}\bar{T}}\left[\frac{\partial\bar{T}}{\partial y}\left(\frac{\partial\tilde{v}}{\partial x}+\frac{\partial\tilde{u}}{\partial y}\right)+\frac{\partial\tilde{T}}{\partial y}\left(\frac{\partial\bar{v}}{\partial x}+\frac{\partial\bar{u}}{\partial y}\right)\right]-\frac{\mathrm{d}\bar{\lambda}}{\mathrm{d}\bar{T}}\left[\frac{\partial\bar{T}}{\partial x}\left(\frac{\partial\tilde{u}}{\partial x}+\frac{\partial\tilde{v}}{\partial y}\right)+\frac{\partial\tilde{T}}{\partial x}\left(\frac{\partial\bar{u}}{\partial x}+\frac{\partial\bar{v}}{\partial y}\right)+\tilde{T}\left(\frac{\partial^2\bar{u}}{\partial x^2}+\frac{\partial^2\bar{v}}{\partial x\partial y}\right)\right]\\
&-\left[\left(\frac{\partial\bar{u}}{\partial y}+\frac{\partial\bar{v}}{\partial x}\right)\frac{\partial\bar{T}}{\partial y}+2\frac{\partial\bar{T}}{\partial x}\frac{\partial\bar{u}}{\partial x}\right]\frac{\partial^2\bar{\mu}}{\partial\bar{T}^2}\tilde{T}-\left(\frac{\partial\bar{u}}{\partial x}+\frac{\partial\bar{v}}{\partial y}\right)\frac{\partial^2\bar{\lambda}}{\partial\bar{T}^2}\frac{\partial\bar{T}}{\partial x}\tilde{T}=0;
\end{aligned}\tag{6}$$

$$\begin{aligned}
&\bar{\rho}\left(\frac{\partial\tilde{v}}{\partial t}+\bar{u}\frac{\partial\tilde{v}}{\partial x}+\tilde{u}\frac{\partial\bar{v}}{\partial x}+\bar{v}\frac{\partial\tilde{v}}{\partial y}+\tilde{v}\frac{\partial\bar{v}}{\partial y}\right)+\tilde{\rho}\left(\bar{u}\frac{\partial\bar{v}}{\partial x}+\bar{v}\frac{\partial\tilde{v}}{\partial y}\right)+\frac{\partial\tilde{p}}{\partial y}-\bar{\mu}\left(\frac{\partial^2\tilde{v}}{\partial x^2}+2\frac{\partial^2\tilde{v}}{\partial y^2}+\frac{\partial^2\tilde{u}}{\partial x\partial y}\right)-\bar{\lambda}\left(\frac{\partial^2\tilde{v}}{\partial y^2}+\frac{\partial^2\tilde{u}}{\partial x\partial y}\right)\\
&-\frac{\mathrm{d}\bar{\mu}}{\mathrm{d}\bar{T}}\left[\left(\frac{\partial\tilde{u}}{\partial y}+\frac{\partial\tilde{v}}{\partial x}\right)\frac{\partial\bar{T}}{\partial x}+\left(\frac{\partial\bar{u}}{\partial y}+\frac{\partial\bar{v}}{\partial x}\right)\frac{\partial\tilde{T}}{\partial x}+\tilde{T}\left(\frac{\partial^2\bar{v}}{\partial x^2}+2\frac{\partial^2\bar{v}}{\partial y^2}+\frac{\partial^2\bar{u}}{\partial x\partial y}\right)+2\left(\frac{\partial\bar{T}}{\partial y}\frac{\partial\tilde{v}}{\partial y}+\frac{\partial\tilde{T}}{\partial y}\frac{\partial\bar{v}}{\partial y}\right)\right]\\
&-\frac{\mathrm{d}\bar{\lambda}}{\mathrm{d}\bar{T}}\left[\frac{\partial\bar{T}}{\partial y}\left(\frac{\partial\tilde{u}}{\partial x}+\frac{\partial\tilde{v}}{\partial y}\right)+\frac{\partial\tilde{T}}{\partial y}\left(\frac{\partial\bar{u}}{\partial x}+\frac{\partial\bar{v}}{\partial y}\right)+\tilde{T}\left(\frac{\partial^2\bar{v}}{\partial y^2}+\frac{\partial^2\bar{u}}{\partial x\partial y}\right)\right]-\left(\frac{\partial\bar{u}}{\partial x}+\frac{\partial\bar{v}}{\partial y}\right)\frac{\partial^2\bar{\lambda}}{\partial\bar{T}^2}\frac{\partial\bar{T}}{\partial y}\tilde{T}\\
&-\left[\left(\frac{\partial\bar{u}}{\partial y}+\frac{\partial\bar{v}}{\partial x}\right)\frac{\partial\bar{T}}{\partial x}+2\frac{\partial\bar{T}}{\partial y}\frac{\partial\bar{v}}{\partial y}\right]\frac{\partial^2\bar{\mu}}{\partial\bar{T}^2}\tilde{T}=0;
\end{aligned}\tag{7}$$

$$\begin{aligned}
&\bar{\rho}C_v\left(\frac{\partial\tilde{T}}{\partial t}+\bar{u}\frac{\partial\tilde{T}}{\partial x}+u'\frac{\partial\bar{T}}{\partial x}+\bar{v}\frac{\partial\tilde{T}}{\partial y}+\tilde{v}\frac{\partial\bar{T}}{\partial y}\right)+\tilde{\rho}C_v\left(\bar{u}\frac{\partial\bar{T}}{\partial x}+\bar{v}\frac{\partial\bar{T}}{\partial y}\right)+\tilde{p}\left(\frac{\partial\bar{u}}{\partial x}+\frac{\partial\bar{v}}{\partial y}\right)+\bar{p}\left(\frac{\partial\tilde{u}}{\partial x}+\frac{\partial\tilde{v}}{\partial y}\right)+\frac{\partial\tilde{q}_x}{\partial x}+\frac{\partial\tilde{q}_y}{\partial y}\\
&-\bar{\tau}_{xx}\frac{\partial\tilde{u}}{\partial x}-\tilde{\tau}_{xx}\frac{\partial\bar{u}}{\partial x}-\left(\frac{\partial\bar{u}}{\partial y}+\frac{\partial\bar{v}}{\partial x}\right)\tilde{\tau}_{xy}-\left(\frac{\partial\tilde{u}}{\partial y}+\frac{\partial\tilde{v}}{\partial x}\right)\bar{\tau}_{xy}-\bar{\tau}_{yy}\frac{\partial\tilde{v}}{\partial y}-\tilde{\tau}_{yy}\frac{\partial\bar{v}}{\partial y}=0;
\end{aligned}\tag{8}$$

$$\frac{\partial\tilde{\rho}}{\partial t}+\bar{\rho}\left(\frac{\partial\tilde{u}}{\partial x}+\frac{\partial\tilde{v}}{\partial y}\right)+\tilde{\rho}\left(\frac{\partial\bar{v}}{\partial y}+\frac{\partial\bar{u}}{\partial x}\right)+\bar{u}\frac{\partial\tilde{\rho}}{\partial x}+\bar{v}\frac{\partial\tilde{\rho}}{\partial y}+\tilde{u}\frac{\partial\bar{\rho}}{\partial x}+\tilde{v}\frac{\partial\bar{\rho}}{\partial y}=0.\tag{9}$$

The heat flux and shear stress tensor components are given below.

$$\tilde{q}_x=-\bar{k}\frac{\partial\tilde{T}}{\partial x}-\tilde{k}\frac{\partial\bar{T}}{\partial x};\quad \tilde{q}_y=-\bar{k}\frac{\partial\tilde{T}}{\partial y}-\tilde{k}\frac{\partial\bar{T}}{\partial y}.$$

$$\tilde{\tau}_{xx}=(2\bar{\mu}+\bar{\lambda})\frac{\partial\tilde{u}}{\partial x}+\bar{\lambda}\frac{\partial\tilde{v}}{\partial y}+(2\tilde{\mu}+\tilde{\lambda})\frac{\partial\bar{u}}{\partial x}+\tilde{\lambda}\frac{\partial\bar{v}}{\partial y};$$

$$\tilde{\tau}_{yy}=(2\bar{\mu}+\bar{\lambda})\frac{\partial\tilde{v}}{\partial y}+\bar{\lambda}\frac{\partial\tilde{u}}{\partial x}+(2\tilde{\mu}+\tilde{\lambda})\frac{\partial\bar{v}}{\partial y}+\tilde{\lambda}\frac{\partial\bar{u}}{\partial x};$$

$$\tilde{\tau}_{xy}=\bar{\mu}\left(\frac{\partial\tilde{u}}{\partial y}+\frac{\partial\tilde{v}}{\partial x}\right)+\tilde{\mu}\left(\frac{\partial\bar{u}}{\partial y}+\frac{\partial\bar{v}}{\partial x}\right).$$

The components of each energy transfer mechanism are mentioned below.

$$\mathrm{P_{RS}} = -\bar{\rho}\left(\tilde{u}\tilde{u}\frac{\partial \bar{u}}{\partial x} + \tilde{u}\tilde{v}\frac{\partial \bar{u}}{\partial y} + \tilde{u}\tilde{v}\frac{\partial \bar{v}}{\partial x} + \tilde{v}\tilde{v}\frac{\partial \bar{v}}{\partial y}\right);$$

$$\mathrm{P_{Conv}} = -\left[\bar{\rho}\bar{u}\left(\tilde{u}\frac{\partial \tilde{u}}{\partial x} + \tilde{v}\frac{\partial \tilde{v}}{\partial x}\right) + \bar{\rho}\bar{v}\left(\tilde{u}\frac{\partial \tilde{u}}{\partial y} + \tilde{v}\frac{\partial \tilde{v}}{\partial y}\right) + \frac{\bar{P}\tilde{T}}{(\gamma-1)\bar{T}^2}\left(\bar{u}\frac{\partial \tilde{T}}{\partial x} + \bar{v}\frac{\partial \tilde{T}}{\partial y}\right) + \frac{\bar{P}\tilde{\rho}}{\bar{\rho}^2}\left(\bar{u}\frac{\partial \tilde{\rho}}{\partial x} + \bar{v}\frac{\partial \tilde{\rho}}{\partial y}\right)\right];$$

$$\mathrm{P_{Mom}} = -\left[\tilde{\rho}\tilde{u}\left(\bar{u}\frac{\partial \bar{u}}{\partial x} + \bar{v}\frac{\partial \bar{u}}{\partial y}\right) + \tilde{\rho}\tilde{v}\left(\bar{u}\frac{\partial \bar{v}}{\partial x} + \bar{v}\frac{\partial \bar{v}}{\partial y}\right)\right];$$

$$\mathrm{P_{Entropy}} = -\left[\bar{\rho}R\left(\frac{\tilde{T}}{(\gamma-1)\bar{T}} - \frac{\tilde{\rho}}{\bar{\rho}}\right)\left(\tilde{u}\frac{\partial \bar{T}}{\partial x} + \tilde{v}\frac{\partial \bar{T}}{\partial y}\right)\right];$$

$$\mathrm{P_{PW}} = -\frac{\tilde{\rho}}{\bar{\rho}}\left(\tilde{u}\frac{\partial \bar{P}}{\partial x} + \tilde{v}\frac{\partial \bar{P}}{\partial y}\right);$$

$$\mathrm{P_{IE}} = -\frac{\tilde{\rho}C_v\tilde{T}}{\bar{T}}\left(\bar{u}\frac{\partial \bar{T}}{\partial x} + \bar{v}\frac{\partial \bar{T}}{\partial y}\right);$$

$$\begin{aligned}\mathrm{P_{TP}} = &\left[\left(2\bar{\mu} - \frac{\mathrm{d}\bar{\mu}}{\mathrm{d}\bar{T}}\bar{T}\right)\left[\frac{\partial \bar{v}}{\partial x}\left(\frac{\partial \tilde{u}}{\partial y} + \frac{\partial \tilde{v}}{\partial x}\right) + \frac{\partial \bar{u}}{\partial y}\left(\frac{\partial \tilde{u}}{\partial y} + \frac{\partial \tilde{v}}{\partial x}\right) + 2\frac{\partial \bar{u}}{\partial x}\frac{\partial \tilde{u}}{\partial x} + 2\frac{\partial \bar{v}}{\partial y}\frac{\partial \tilde{v}}{\partial y}\right]\right.\\
&+\left(2\bar{\lambda} - \frac{\mathrm{d}\bar{\lambda}}{\mathrm{d}\bar{T}}\bar{T}\right)\left(\frac{\partial \bar{v}}{\partial y} + \frac{\partial \bar{u}}{\partial x}\right)\left(\frac{\partial \tilde{u}}{\partial x} + \frac{\partial \tilde{v}}{\partial y}\right) + \tilde{T}\frac{\mathrm{d}\bar{\mu}}{\mathrm{d}\bar{T}}\left[2\left(\frac{\partial \bar{u}}{\partial x}\right)^2 + 2\left(\frac{\partial \bar{v}}{\partial y}\right)^2 + \left(\frac{\partial \bar{v}}{\partial x}\right)^2 + \left(\frac{\partial \bar{u}}{\partial y}\right)^2 + 2\frac{\partial \bar{u}}{\partial y}\frac{\partial \bar{v}}{\partial x}\right] +\\
&\left.\frac{\mathrm{d}\bar{\lambda}}{\mathrm{d}\bar{T}}\tilde{T}\left[\left(\frac{\partial \bar{u}}{\partial x}\right)^2 + \left(\frac{\partial \bar{v}}{\partial y}\right)^2 + 2\frac{\partial \bar{u}}{\partial x}\frac{\partial \bar{v}}{\partial y}\right] + \frac{\bar{k}}{\bar{T}}\left(\frac{\partial \bar{T}}{\partial x}\frac{\partial \tilde{T}}{\partial x} + \frac{\partial \bar{T}}{\partial y}\frac{\partial \tilde{T}}{\partial y}\right) + \left[\frac{\partial}{\partial x}\left(\tilde{T}\frac{\mathrm{d}\bar{k}}{\mathrm{d}\bar{T}}\frac{\partial \bar{T}}{\partial x}\right) + \frac{\partial}{\partial y}\left(\tilde{T}\frac{\mathrm{d}\bar{k}}{\mathrm{d}\bar{T}}\frac{\partial \bar{T}}{\partial y}\right)\right]\right]\frac{\tilde{T}}{\bar{T}};\end{aligned}$$

$$\mathrm{P_{Dila}} = -\left(\frac{\tilde{P}\tilde{T}}{\bar{T}} + \frac{\bar{P}\tilde{\rho}^2}{\bar{\rho}^2}\right)\left(\frac{\partial \bar{u}}{\partial x} + \frac{\partial \bar{v}}{\partial y}\right);$$

$$\mathrm{D_{SW}} = -\left[\tilde{\tau}_{xx_1}\frac{\partial \tilde{u}}{\partial x} + \tilde{\tau}_{yy_1}\frac{\partial \tilde{v}}{\partial y} + \tilde{\tau}_{xy_1}\left(\frac{\partial \tilde{v}}{\partial x} + \frac{\partial \tilde{u}}{\partial y}\right)\right];$$

$$\mathrm{D_{Cond}} = -\left(\tilde{q}_{x_1}\frac{\partial \tilde{T}}{\partial x} + \tilde{q}_{y_1}\frac{\partial \tilde{T}}{\partial y}\right);$$

$$\begin{aligned}\mathrm{F_{TP}} = -\Bigg[&2\frac{\partial}{\partial x}\left(\tilde{\mu}\tilde{u}\frac{\partial \bar{u}}{\partial x}\right) + \frac{\partial}{\partial x}\left(\tilde{\lambda}\tilde{u}\frac{\partial \bar{u}}{\partial x}\right) + \frac{\partial}{\partial x}\left(\tilde{\mu}\tilde{v}\frac{\partial \bar{v}}{\partial x}\right) + \frac{\partial}{\partial y}\left(\tilde{\mu}\tilde{u}\frac{\partial \bar{u}}{\partial y}\right) + \frac{\partial}{\partial x}\left(\tilde{\mu}\tilde{v}\frac{\partial \bar{u}}{\partial y}\right) + \frac{\partial}{\partial x}\left(\tilde{\lambda}\tilde{u}\frac{\partial \bar{v}}{\partial y}\right)\\
&+\frac{\partial}{\partial y}\left(\tilde{\lambda}\tilde{v}\frac{\partial \bar{v}}{\partial y}\right) + 2\frac{\partial}{\partial y}\left(\tilde{\mu}\tilde{v}\frac{\partial \bar{v}}{\partial y}\right) + \frac{\partial}{\partial y}\left(\tilde{\lambda}\tilde{v}\frac{\partial \bar{u}}{\partial x}\right) + \frac{\partial}{\partial y}\left(\tilde{\mu}\tilde{u}\frac{\partial \bar{v}}{\partial x}\right)\Bigg];\end{aligned}$$

$$\mathrm{F_{PW}} = -\left[\tilde{P}\left(\frac{\partial \tilde{u}}{\partial x} + \frac{\partial \tilde{v}}{\partial y}\right) + \tilde{u}\frac{\partial \tilde{P}}{\partial x} + \tilde{v}\frac{\partial \tilde{P}}{\partial y}\right];$$

$$\mathrm{F_{HF}} = -\left[\frac{\partial}{\partial x}\left(\frac{\bar{k}\tilde{T}}{\bar{T}}\frac{\partial \tilde{T}}{\partial x}\right) + \frac{\partial}{\partial y}\left(\frac{\bar{k}\tilde{T}}{\bar{T}}\frac{\partial \tilde{T}}{\partial y}\right)\right];$$

$$\mathrm{F_{SW}} = \frac{\partial}{\partial x}\left(\tilde{u}\tilde{\tau}_{xx_1}\right) + \frac{\partial}{\partial y}\left(\tilde{v}\tilde{\tau}_{yy_1}\right) + \frac{\partial}{\partial x}\left(\tilde{v}\tilde{\tau}_{xy_1}\right) + \frac{\partial}{\partial y}\left(\tilde{u}\tilde{\tau}_{xy_1}\right).$$

The heat flux and stress tensor can be written as,

$$\tilde{q}_{x_1} = -\bar{k}\frac{\partial \tilde{T}}{\partial x}; \quad \tilde{q}_{y_1} = -\bar{k}\frac{\partial \tilde{T}}{\partial y}.$$

$$\tilde{\tau}_{xx_1} = (2\bar{\mu} + \bar{\lambda})\frac{\partial \tilde{u}}{\partial x} + \bar{\lambda}\frac{\partial \tilde{v}}{\partial y};$$

$$\tilde{\tau}_{yy_1} = (2\bar{\mu} + \bar{\lambda})\frac{\partial \tilde{v}}{\partial y} + \bar{\lambda}\frac{\partial \tilde{u}}{\partial x};$$

$$\tilde{\tau}_{xy_1} = \bar{\mu}\left(\frac{\partial \tilde{u}}{\partial y} + \frac{\partial \tilde{v}}{\partial x}\right).$$

References

[1] Schneider, S. P., "Hypersonic boundary-layer transition with ablation and blowing," Journal of Spacecraft and Rockets, Vol. 47, No. 2, 2010, pp. 225–237.

[2] Schneider, S. P., "Summary of hypersonic boundary-layer transition experiments on blunt bodies with roughness," Journal of Spacecraft and Rockets, Vol. 45, No. 6, 2008, pp. 1090–1105.

[3] Choudhari, M., Li, F., Chang, C.-L., Edwards, J., Kegerise, M., and King, R., "Laminar-Turbulent Transition behind Discrete Roughness Elements in a High-Speed Boundary Layer," 48th AIAA aerospace sciences meeting including the new horizons forum and aerospace exposition, 2010, p. 1575.

[4] Choudhari, M. M., Li, F., Bynum, M. D., Kegerise, M. A., and King, R. A., "Computations of disturbance amplification behind isolated roughness elements and comparison with measurements," 45th AIAA Fluid Dynamics Conference, 2015, p. 2625.

[5] Hein, S., Theiss, A., Di Giovanni, A., Stemmer, C., Schilden, T., Schröder, W., Paredes, P., Choudhari, M. M., Li, F., and Reshotko, E., "Numerical investigation of roughness effects on transition on spherical capsules," Journal of spacecraft and rockets, Vol. 56, No. 2, 2019, pp. 388–404.

[6] Iyer, P., Muppidi, S., and Mahesh, K., "Roughness-induced transition in high speed flows," 49th AIAA Aerospace Sciences Meeting including the New Horizons Forum and Aerospace Exposition, 2011, p. 566.

[7] Shrestha, P., and Candler, G. V., "Direct numerical simulation of high-speed transition due to roughness elements," Journal of Fluid Mechanics, Vol. 868, 2019, pp. 762–788.

[8] Marxen, O., Iaccarino, G., and Shaqfeh, E. S., "Disturbance evolution in a Mach 4.8 boundary layer with two-dimensional roughness-induced separation and shock," Journal of Fluid Mechanics, Vol. 648, 2010, p. 435.

[9] Novikov, A., Egorov, I., and Fedorov, A., "Direct numerical simulation of supersonic boundary layer stabilization using grooved wavy surface," 48th AIAA Aerospace Sciences Meeting Including the New Horizons Forum and Aerospace Exposition, 2010, p. 1245.

[10] Duan, L., Wang, X., and Zhong, X., "A high-order cut-cell method for numerical simulation of hypersonic boundary-layer instability with surface roughness," Journal of computational physics, Vol. 229, No. 19, 2010, pp. 7207–7237.

[11] Duan, L., Wang, X., and Zhong, X., "A High Order Cut-Cell Method for Numerical Simulation of Hypersonic-Boundary Transition with Arbitrary Surface Roughness," 47th AIAA Aerospace Sciences Meeting including The New Horizons Forum and Aerospace Exposition, 2009, p. 1337.

[12] Fong, K. D., Wang, X., and Zhong, X., "Numerical simulation of roughness effect on the stability of a hypersonic boundary layer," Computers & Fluids, Vol. 96, 2014, pp. 350–367.

[13] Fong, K. D., and Zhong, X., "DNS and PSE study on the stabilization effect of hypersonic boundary layer waves using 2-D surface roughness," 46th AIAA Fluid Dynamics Conference, 2016, p. 3347.

[14] Fong, K. D., Wang, X., and Zhong, X., "Parametric study on stabilization of hypersonic boundary layer waves using 2-D surface roughness," 53rd AIAA Aerospace Sciences Meeting, 2015, p. 0837.

[15] Zhou, Y., Liu, W., Chai, Z., and Yang, X., "Numerical simulation of wavy surface effect on the stability of a hypersonic boundary layer," Acta Astronautica, Vol. 140, 2017, pp. 485–496.

[16] Poplavskaya, T., and Kirilovskiy, S., "Numerical investigation of the influence of the structured surface on disturbance evolution and heat transfer in a hypersonic boundary layer," AIP Conference Proceedings, Vol. 2027, AIP Publishing LLC, 2018, p. 030019.

[17] Di Giovanni, A., and Stemmer, C., "Direct Numerical Simulations of roughness-induced transition in the boundary layer of a hypersonic spherical forebody under consideration of high-temperature gas effects," 2018 Fluid Dynamics Conference, 2018, p. 4046.

[18] Di Giovanni, A., and Stemmer, C., "Roughness-induced boundary-layer transition on a hypersonic capsule-like forebody including nonequilibrium," Journal of Spacecraft and Rockets, Vol. 56, No. 6, 2019, pp. 1795–1808.

[19] Holloway, P. F., and Sterrett, J. R., "Effect of controlled surface roughness on boundary-layer transition and heat transfer at mach numbers of 4.8 and 6.0," TN D-2054, NASA, April,1964.

[20] Fujii, K., "Experiment of the two-dimensional roughness effect on hypersonic boundary-layer transition," Journal of Spacecraft and Rockets, Vol. 43, No. 4, 2006, pp. 731–738.

[21] Browne, O. M., Haas, A. P., Fasel, H. F., and Brehm, C., "An efficient linear wavepacket tracking method for hypersonic boundary-layer stability prediction," Journal of Computational Physics, Vol. 380, 2019, pp. 243–268. https://doi.org/10.1016/j.jcp.2018.11.028.

[22] Browne, O. M., Haas, A. P., Fasel, H. F., and Brehm, C., "A Nonlinear Wavepacket Tracking Method for Hypersonic Boundary-Layer Flows on Irregular Domains," AIAA Aviation 2020 Forum, 2020, p. 2985. https://doi.org/10.2514/6.2020-2985.

[23] Brehm, C., Barad, M. F., Housman, J. A., and Kiris, C. C., "A comparison of higher-order finite-difference shock capturing schemes," Computers & Fluids, Vol. 122, 2015, pp. 184–208. https://doi.org/10.1016/j.compfluid.2015.08.023.

[24] Schneider, S. P., "Effects of roughness on hypersonic boundary-layer transition," Journal of Spacecraft and Rockets, Vol. 45, No. 2, 2008, pp. 193–209.

[25] Chu, B.-T., "On the energy transfer to small disturbances in fluid flow (Part I)," Acta Mechanica, Vol. 1, No. 3, 1965, pp. 215–234.

[26] Bountin, D., Chimitov, T., Maslov, A., Novikov, A., Egorov, I., Fedorov, A., and Utyuzhnikov, S., "Stabilization of a hypersonic boundary layer using a wavy surface," AIAA journal, Vol. 51, No. 5, 2013, pp. 1203–1210.